Kinematic analysis of the Pakuashan fault tip fold, Western central Taïwan : Shortening rate and age of folding inception

Martine Simoes, Jean-Philippe Avouac, Yue-Gau Chen, Ashok K. Singhvi, Chien-Ying Wang, Manoj Aiswal, Yu-Chang Chan, Sylvain Bernard

Kinematic analysis of the Pakuashan fault tip fold, west central Taiwan: Shortening rate and age of folding inception

Martine Simoes,[1,2,3] Jean Philippe Avouac,[1] Yue-Gau Chen,[4] Ashok K. Singhvi,[5] Chien-Ying Wang,[6] Manoj Jaiswal,[5,7,8] Yu-Chang Chan,[9] and Sylvain Bernard[2]

Received 30 November 2005; revised 2 October 2006; accepted 15 December 2006; published 13 February 2007.

[1] The Pakuashan anticline is an active fault tip fold that constitutes the frontal most zone of deformation along the western piedmont of the Taiwan Range. Assessing seismic hazards associated with this fold and its contribution to crustal shortening across central Taiwan requires some understanding of the fold structure and growth rate. To address this, we surveyed the geometry of several deformed strata and geomorphic surfaces, which recorded different cumulative amounts of shortening. These units were dated to ages ranging from ~19 ka to ~340 ka using optically stimulated luminescence (OSL). We collected shallow seismic profiles and used previously published seismic profiles to constrain the deep structure of the fold. These data show that the anticline has formed as a result of pure shear with subsequent limb rotation. The cumulative shortening along the direction of tectonic transport is estimated to be 1010 ± 160 m. An analytical fold model derived from a sandbox experiment is used to model growth strata. This yields a shortening rate of 16.3 ± 4.1 mm/yr and constrains the time of initiation of deformation to 62.2 ± 9.6 ka. In addition, the kinematic model of Pakuashan is used to assess how uplift, sedimentation, and erosion have sculpted the present-day fold topography and morphology. The fold model, applied here for the first time on a natural example, appears promising in determining the kinematics of fault tip folds in similar contexts and therefore in assessing seismic hazards associated with blind thrust faults.

Citation: Simoes, M., J. P. Avouac, Y.-G. Chen, A. K. Singhvi, C.-Y. Wang, M. Jaiswal, Y.-C. Chan, and S. Bernard (2007), Kinematic analysis of the Pakuashan fault tip fold, west central Taiwan: Shortening rate and age of folding inception, *J. Geophys. Res.*, *112*, B03S14, doi:10.1029/2005JB004198.

1. Introduction

[2] Taiwan is located at the boundary between the Philippine Sea Plate and the Eurasian Plate. The GPS-based plate tectonic model REVEL [*Sella et al.*, 2002] indicates that the convergence rate is of ~90 mm/yr in a NW-SE direction (Figure 1). A fraction of this convergence is absorbed by crustal shortening across the Taiwanese range, west of the Longitudinal Valley suture zone. Progradation of sediments over the flexed foreland suggests a shortening rate of 39.5–44.5 mm/yr across the range over the last ~2 Myr, and this shortening appears to be mostly (if not totally) taken up by slip on the thrust faults of the western foothills [*Simoes and Avouac*, 2006]. These faults are the Chelungpu fault which broke during the 1999 ChiChi earthquake [*Ma et al.*, 1999] (Figure 2), the Shuangtung, the Chushiang and the Changhua faults [*Bonilla*, 1975, 1999; *Chen et al.*, 2004; *Shyu et al.*, 2005; *Tsai*, 1985]. Except for the Chelungpu and Chushiang faults whose shortening rates have been recently estimated in the region of the Choushui Hsi river (Figure 2) [*Simoes et al.*, 2007], the contribution of the other structures to crustal shortening across the Taiwanese range is not yet resolved [e.g., *Cattin et al.*, 2004]. This study focuses on the Changhua thrust fault, which is the frontal most fault of central Taiwan (Figures 1 and 2), and which is presently the primary source of seismic hazards in this densely populated area [*Lee and Lin*, 2004]. This fault is blind [*Delcaillau et al.*, 1998] and recent tectonic activity is evidenced from the ubiquitous presence of tilted geomorphic markers (Figures 3–5). The shortening rate and the age of folding inception are yet unresolved. In general, deciphering the kinematics of a fold formed above a blind fault, as is the case here, is reputably difficult. The structural expression of folding can be subtle and dating of the folded

[1] Tectonics Observatory, California Institute of Technology, Pasadena, California, USA.
[2] Laboratoire de Géologie, CNRS, Ecole Normale Supérieure, Paris, France.
[3] Now at Géosciences Rennes, CNRS, Université Rennes 1, Rennes, France.
[4] Department of Geosciences, National Taiwan University, Taipei, Taiwan.
[5] Planetary and Geosciences Division, Physical Research Laboratory, Ahmedabad, India.
[6] Institute of Geophysics, National Central University, Jhongli, Taiwan.
[7] Also at Wadia Institute of Himalayan Geology, Dehradun, India.
[8] Now at Department of Geosciences, National Taiwan University, Taipei, Taiwan.
[9] Institute of Earth Sciences, Academia Sinica, Taipei, Taiwan.

0148-0227/07/2005JB004198$09.00

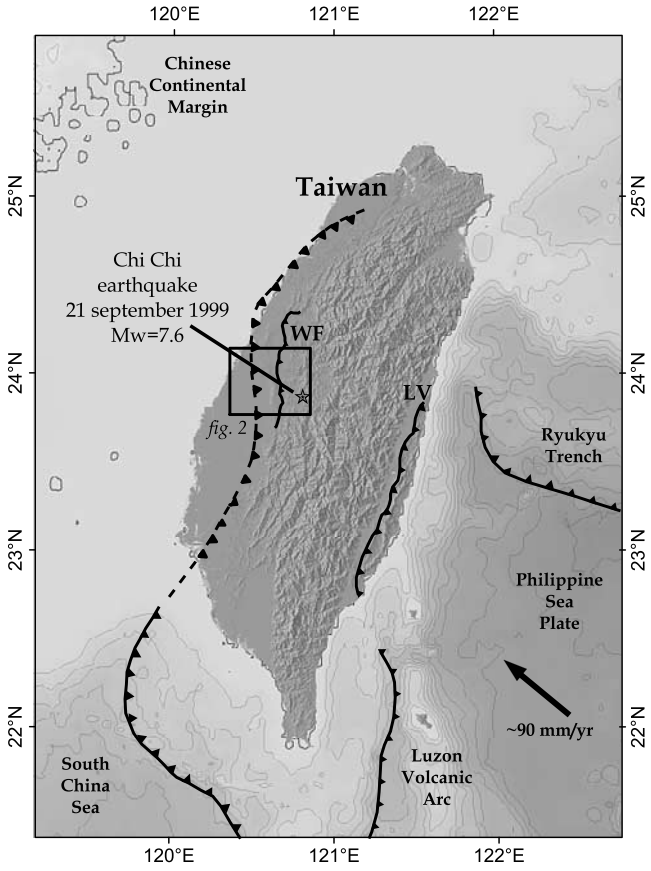

Figure 1. Geodynamical setting of Taiwan. Thick arrow shows the convergence of the Philippine Sea Plate relative to the Chinese Continental Margin predicted from the GPS-derived REVEL plate model [*Sella et al.*, 2002]. The Longitudinal Valley (LV) marks the suture between the two plates. Also illustrated are the ChiChi earthquake epicenter and surface fault rupture [e.g., *Ma et al.*, 1999]. Inset locates our study area within the Western Foothills (WF), illustrated in more detail in Figure 2.

layers is often challenging. In addition, determining the kinematics of folding on a blind fault requires a fold model [e.g., *Shaw et al.*, 2002], and the choice of the most appropriate model is generally non trivial (Figure 3). In this study, the finite structure of the fold is documented from existing seismic profiles and from new shallow seismic profiles (Figure A1), and is used to calibrate an analytical fold model [*Bernard et al.*, 2007] derived from analogue modeling [*Dominguez et al.*, 2003b]. This is the first application of this fold model to a natural setting. The fold model allows for retrieving the deformation history from growth strata and deformed fluvial terraces, which were surveyed in the field and dated using optically stimulated luminescence (OSL) (Figures 4–7).

2. Geological Setting

2.1. Evidence for Recent Activity and Morphology of the Pakuashan Anticline

[3] Geodetic data [*Yu et al.*, 1997] show that the Changhua fault was primarily locked before the 1999 Chi-Chi earthquake [*Dominguez et al.*, 2003a; *Hsu et al.*, 1998; *Loevenbruck et al.*, 2001]. Evidence for a few centimeters creep on the Changhua fault triggered by this earthquake was observed from radar interferometry [*Pathier et al.*, 2003], but it seems probable that the fault mostly breaks during large earthquakes, such as the 1848 $M_w \sim 7.1$ Changhua earthquake [*Tsai*, 1985] (Figure 2). The Tatushan and Pakuashan anticlines are the geomorphic and structural expressions of deformation associated with slip on the Changhua blind thrust fault (Figure 2). They form an elongated ridge extending over ~80 km from north to south, with a mean elevation of ~250–300 m, and a maximum elevation of ~400 m to the south. East of these anticlines, the Taichung basin is a typical piggyback basin (Figure 2).

[4] The curvature of the Pakuashan anticline (Figure 2) is attributed to the geometry of the underthrusting basement [*Mouthereau et al.*, 1999]. Seismic profiles show in particular that this fold has developed above an ancient normal fault that separates the Peikang High from the Taichung basin [e.g., *Chang*, 1971; *Chen*, 1978] (Figure 8). Normal faults in the basement are thought to be related to Paleocene rifting and Oligocene opening of the South China Sea, and were possibly reactivated during the Taiwan orogeny due to flexural bending of the foreland [*Chou and Yu*, 2002]. Reactivation is suggested by the presence of ~2–3 Ma deep offshore deposits (Cholan Formation) in the footwall of this hinge fault [*Covey*, 1984a, 1984b], and by strong lateral variations in the thickness of late Pliocene deposits (Figure 8). Younger deposits do not show lateral variations in thickness across the hinge fault. This implies that activity of this normal fault ceased most probably by early Pleistocene. The Pakuashan anticline is unconformably capped by lateritic fluvial deposits (Figures 2, 4, and 6), which have not yet been precisely dated but are thought to be younger than ~350 ka [*Liew*, 1988]. At places, several imbricate fluvial terraces separated by terrace risers can be distinguished. They provide evidence for recent activity of the Changhua thrust fault and for limb rotation during recent incremental folding (Figures 3–5). An implication is that the folding mechanism probably involves some component of pure shear deformation (Figure 3). The north-south variation of the morphology of the Pakuashan anticline (Figure 2) has been interpreted to reflect a southward propagation of deformation [*Delcaillau et al.*, 1998]. Various authors have suggested variable estimates of the cumulative shortening across the Pakuashan anticline: ~500 m [*Mouthereau et al.*, 1999], 700 m [*Yue et al.*, 2005] or ~4 km [*Delcaillau*, 2001]. Likewise, the age of folding inception and the shortening rate absorbed by the Changhua fault are not well constrained.

2.2. Stratigraphy

[5] The Pakuashan anticline is deforming sediments initially deposited in the foreland basin west of Taiwan (Figure 8). The Mesozoic basement is overlain by a thick Cenozoic sedimentary cover, which is relatively well documented in earlier geophysical and stratigraphic studies [e.g., *Chang*, 1971; *Chen*, 1978; *Covey*, 1984a, 1986; *Hung and Suppe*, 2002; *Lin et al.*, 2003; *Wang et al.*, 2003, 2002] (Figures 2, 4, and 6). The chronostratigraphy of the series was established from calcareous nannoplankton [*Chang*

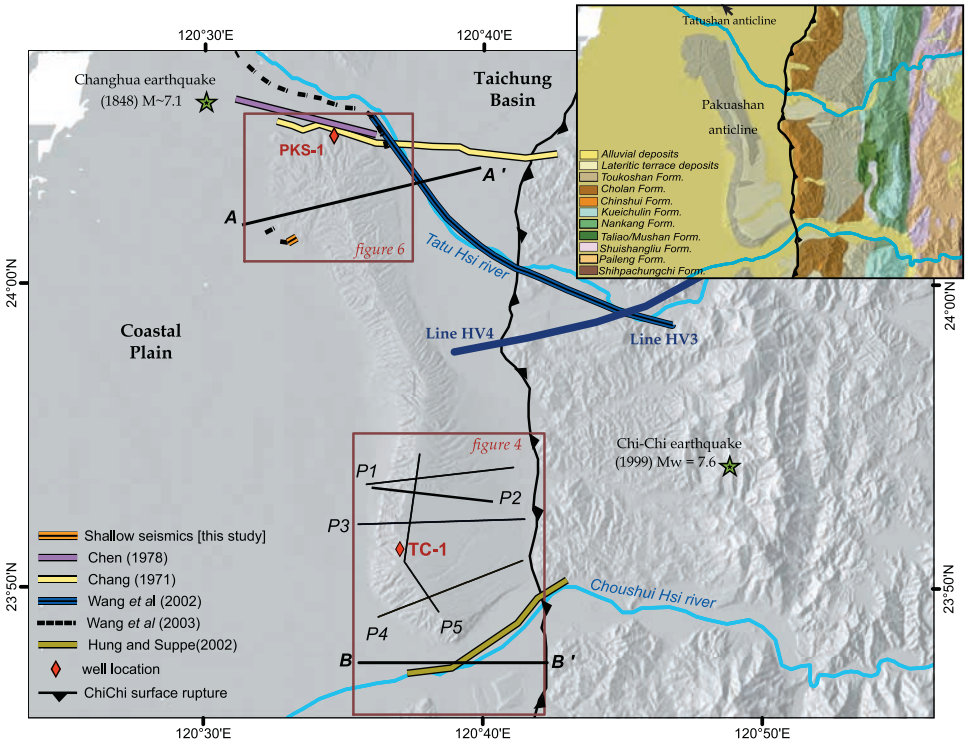

Figure 2. Map of the Western Foothills of central Taiwan with locations of PKS-1 and TC-1 wells, along with available seismic lines [*Chang*, 1971; *Chen*, 1978; *Hung and Suppe*, 2002; *Wang et al.*, 2003, 2002]. The Changhua blind fault marks the front of the Taiwan range in this region and is responsible for folding of the Pakuashan and Tatushan anticlines. The location of the shallow seismic profiles collected in this study (shown in more detail in Figures 6 and A1) is also indicated. P1 to P5 show location of topographic profiles across lateritic surfaces which cap the anticline to the south; they are reported in Figure 5. Lines A-A′ and B-B′ indicate the N78° ± 3°E and N90° ± 5°E directions along which data are projected for northern and southern Pakuashan, respectively. Boxes show the locations of Figures 4 and 6. Inset presents a simplified geological map of same area.

and Chi, 1983] and plankton foraminifera [*Huang*, 1984] and is calibrated using magnetostratigraphy [*Horng and Shea*, 1996]. Paleocene to late Miocene series of continental China affinity were deposited during an early rifting phase, from ~57 to 30 Ma, and during the opening of the South China Sea, from ~30 to 6.5 Ma [e.g., *Briais et al.*, 1993; *Lin et al.*, 2003]. According to *Lin et al.* [2003], the late Miocene (~6.5 Ma) basal unconformity marks the onset of the development of the foreland basin, and thus provides an age for initiation of the collision between the Luzon Arc and the Chinese Continental Margin. The late Miocene Kueichulin Formation, essentially composed of sandstones intercalated with sandy shales, is the first synorogenic sedimentary unit. It is conformably overlain by the Pliocene thin shales and siltstones of the Chinshui Formation. Above, the upper Pliocene Cholan Formation is constituted of light gray to brownish shales, intercalated with fine to coarse sandy layers. Upward in the section, the Toukoshan Formation forms a thick synorogenic Plio-Pleistocene clastic sequence, mainly composed of sandy sediments from braided rivers and deltaic environments trending upward to conglomerate river assemblages including sandstone lenses. Seismic profiles across the Pakuashan anticline suggest that all this Plio-Pleistocene sequence is conformable, and that it was deposited before shortening on the Changhua fault began (Figure 8).

[6] These pregrowth deposits are unconformably overlain by lateritic fluvial terraces [*Teng*, 1987], mostly preserved along the axial line zone and on the backlimb of central and southern Pakuashan (Figures 2 and 4). To the north, smaller patches can still be observed along the backlimb (Figure 6). Since they postdate the last observed deposits of the Toukoshan Formation, these terraces are younger than ~0.5 Ma. *Liew* [1988] argues that they were deposited during a period of rising sea level possibly by 0.35 Ma, and that weathering has possibly occurred during the major transgression related to the Late Interglacial event 0.13 Myr ago. In addition, other recent alluvial sediments were deposited unconformably above the pretectonic strata on both sides of the Pakuashan anticline.

2.3. Pregrowth Sedimentation Rates

[7] Sedimentation rates within the proximal foreland basin reflect the sedimentation history before initiation of shortening on the Changhua fault. To assess these rates, we use data from the PKS-1 well [*Chang*, 1971] in northern Pakuashan (Figures 2 and 6), for which a detailed analysis of sedimentary facies and nannostratigraphy is available [*Covey*, 1984b]. Nannoplankton zones are converted into

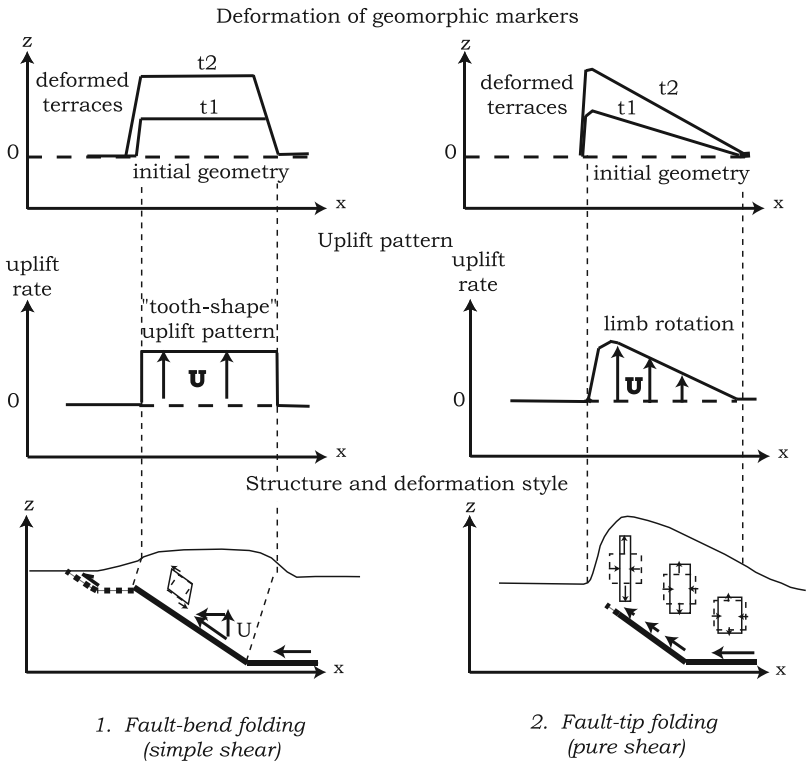

Figure 3. Sketch showing the deformation of geomorphic markers during the incremental growth (left) of a fault bend fold and (right) of a fault tip fold. In the case of a fault bend fold [*Suppe*, 1983], the fault may emerge at the surface or ramp to a shallower decollement. The pattern of uplift is simple and is directly a function of the fault dip angle [*Lavé and Avouac*, 2000]. In the case of a fault tip fold, slip tapers to zero at the tip of the fault and the fold deformation pattern is more complex. We present here the case where deformation is absorbed by pure shear, inducing limb rotation. The pattern of incremental deformation as retrieved from deformed geomorphic markers or growth strata may help discriminate the mode of folding.

calendar ages based on the paleomagnetic calibration of *Horng and Shea* [1996]. This calibration provides results consistent with those inferred from other calibrated biostratigraphic timescales [*Berggren*, 1973; *Berggren et al.*, 1995]. Sediment thicknesses in PKS-1 are decompacted using *Audet*'s [1995] porosity-depth relation with the parameters inferred in the offshore foreland basin by *Lin et al.* [2003] for the BD1 well. Burial depths are estimated taking into account ~300 m of erosion at the top of the sedimentary sequence [*Covey*, 1984b]. The calculated sedimentation rates increase upward (Figure 9), which is consistent with the progressive migration of the orogen to the west over its foreland [*Covey*, 1984a; *Simoes and Avouac*, 2006]. Sedimentation rates reach ~2.2 to 2.8 mm/yr over the last ~1 Myr in PKS-1, a value similar to the ~2–3 mm/yr subsidence rate averaged over the Holocene time period and documented west of Pakuashan [*Lai and Hsieh*, 2003].

3. Subsurface Structure of the Pakuashan Anticline

3.1. Seismic Profiles and Well Data Analysis

[8] Available seismic profiles and well logs are georeferenced to a 40-m DEM and projected on a section perpendicular to the fold axis. The fold axis direction, N168° ± 3°E for the northern area and N0 ± 5°E for the southern area, is determined by fitting the tilt of the lateritic terraces preserved on the backlimb with planar surfaces using a least squares criterion. Note that the seismic profiles used here to constrain the subsurface geometry of the Pakuashan anticline have been previously interpreted in the different source papers. The earlier interpretation lines can look like reflectors and can therefore be misleading.

3.1.1. Northern Section

[9] Several seismic profiles are available for the northern section of the Pakuashan anticline. *Chen*'s [1978] profile runs along the TaTu river, 2 to 8 km to the north of our study area (Figures 2 and 6). We converted the traveltimes, as provided in the original interpreted profile, to depths using the average velocities inferred from well shooting on PKS-1 [*Chen*, 1978] and from seismic refraction investigations in the same region [*Sato et al.*, 1970] (see details in Appendix A). Although approximate, our conversion predicts depths consistent with those observed in the well PKS-1 (Figure 8 and Appendix A). Seismic investigations by *Chang* [1971] in the Taichung basin complement the former profile further east. Chang, however, did not describe the velocities used for depth conversion, and we assume that the velocities measured within the PKS-1 well or retrieved from earlier refraction investigations [*Sato et al.*, 1970] were used. A good geometrical continuity is observed between

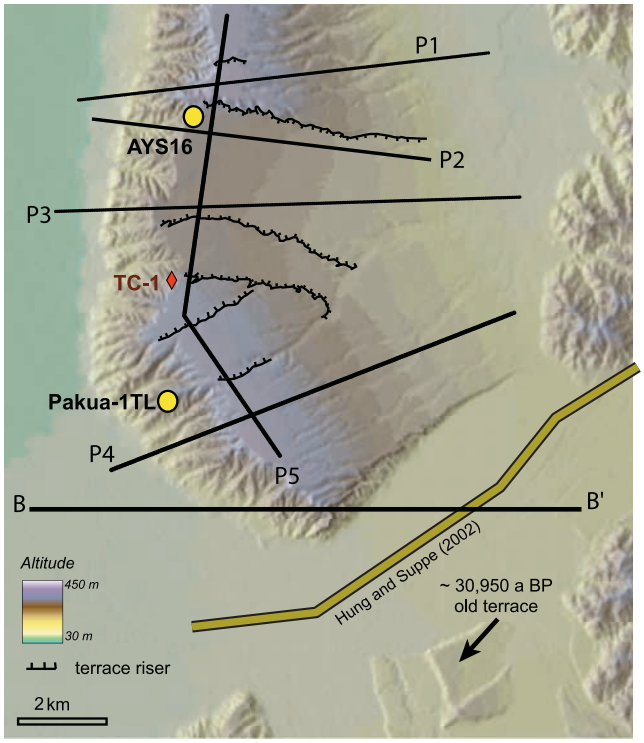

Figure 4. Map of southern Pakuashan (see location in Figure 2). All data were projected onto section B-B′, which is perpendicular to the fold axis. The strath of the fluvial terrace dated to 30,950 ± 290 years B.P. by radiocarbon [*Ota et al.*, 2002] was surveyed in the field (see strath profile in Figure 5a). OSL samples Pakua1-TL and AYS16 date lateritic terraces P2 and P4 to 19,000 ± 4000 years and 19,000 ± 2000 years, respectively (Table 2 and Appendix C).

this profile with the one from *Chen* [1978], despite a slight difference in the estimated depth of the top of the Cholan Formation. This most certainly relates to the smearing out of the reflector in *Chang*'s [1971] profile beneath the Pakuashan anticline. A rigorous match between the two profiles is not possible in the strictest sense, but *Chang*'s [1971] seismic profile still provides some information on the pattern of deformation at the eastern end of the backlimb (Figure 8). Below the Taichung basin and further east, the subsurface is imaged by *Wang et al.*'s [2002] profile (Figures 2 and 8). The velocities used for depth conversion are in this case ∼10% higher than those known in the western plain area and used to convert *Chen*'s [1978] profile. This correction applies mainly for the shallower strata, and is probably not appropriate for levels below ∼4200 m. The apparent continuity of the well-stratified reflectors at the base of the Toukoshan formation between *Chen*'s [1978] and *Wang et al.*'s [2002] profiles supports this inference (Figure 8). The Plio-Pleistocene strata show dips gentler than beneath Pakuashan, so that this profile puts constraints on the eastern limit of the fold width (Figure 8). Therefore errors in depths and dips induced by our correction are not expected to affect much our analysis.

[10] We have also used *Wang et al.*'s [2003] shallow seismic profiles along the Tatu Hsi (Figures 2 and 8). Lateral variations in the structures can occur between the Tatu Hsi and the transect investigated in the field, as suggested by the forefront fold morphology (Figure 6). Therefore we conducted shallow seismic investigations (seismic lines W1, L1 and L2, Figures 6 and A1) on the frontalmost portion of the Pakuashan anticline in our field area. Details are presented in Appendix A. We mainly rely on lines W1 and L1 closer to the section investigated in the field (Figure 6).

3.1.2. Southern Section

[11] The subsurface structure of southern Pakuashan was imaged by *Hung and Suppe*'s [2002] seismic profile along the Choushui Hsi (Figure 4). Hereafter we use the interpreted version of this profile, already converted to depths, as in Figure 4b of *Yue et al.* [2005] (Figure 10). This profile is compared to the TC-1 well log (J.-H. Hung, personal communication, 2005) (Figure 4) to estimate uncertainties on depths and dips retrieved from the profile (see Appendix A for details).

3.2. Constraints on the Subsurface Geometry of the Changhua Fault

[12] The repetition of a 380–420 m thick sequence of the Cholan Formation along PKS-1 indicates that the fault lies at a depth of ∼2800 m below the core of the Pakuashan anticline [*Chen*, 1978] (red star in Figure 8). This location is consistent with the seismic profile of Figure 8, which shows that all the layers above this depth are folded while those below are not. Updip of this intersection, the fault can be traced up to the depth of ∼1700 m below the forelimb. This also holds for southern Pakuashan (Figure 10). At shallower depths, most horizons are continuous showing that the Changhua fault does not reach the surface (Figure 8). One possibility would be that the fault would ramp to a decollement within the stratigraphic sequence at a depth of ∼1700 m. In this case, the fold would be a fault bend fold [*Suppe*, 1983] over a blind ramp. However, there is no indication of significant deformation transferred to the west of the Pakuashan anticline (Figure 2). We therefore rather favor the hypothesis that the Pakuashan anticline formed at the blind tip of the leading edge of the Changhua fault.

[13] Downdip of the intersection with PKS-1 it is rather difficult to estimate the Changhua fault's geometry directly from the seismic line. One possibility is that the fault roots into some decollement at a level as shallow as its intersection with PKS-1. *Chen* [1978] proposes that the Changhua decollement roots within the Cholan formation, at ∼2700–3000 m depth beneath the Taichung Basin. However, this interpretation is inconsistent with independent geometrical observations. There is good evidence that the Chinshui Shales, at ∼4200 m depth beneath the Taichung Basin [*Chang*, 1971], are the decollement level of the Chelungpu fault further east [e.g., *Yue et al.*, 2005] (Figures 2 and 11). If we admit *Chen*'s [1978] interpretation, the Changhua decollement would connect to the ramp of the Chelungpu fault. In this case, the junction is geometrically unstable, and any significant slip on the Changhua fault would require a kink in the ramp of the Chelungpu fault. No such clues are observed on the seismic lines of *Wang et al.* [2002] along the Tatu and the Choushui Hsi (Figure 11). It is therefore most probable that the Changhua and the Chelungpu faults

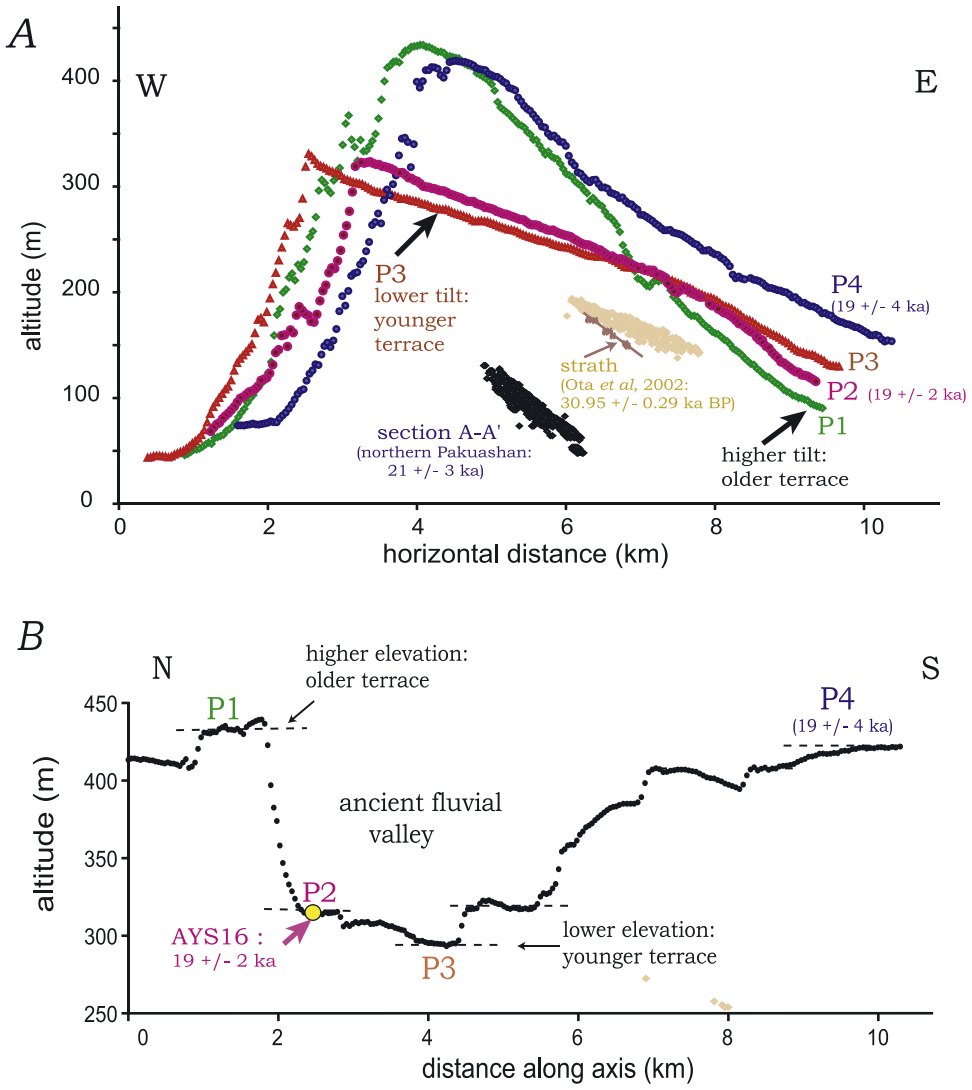

Figure 5. Profiles of tilted geomorphic surfaces across northern (section AA′) and southern (section BB′) Pakuashan. See Figures 2 and 4 for location of profiles P1 to P5. (a) Profiles perpendicular to the fold axis showing progressive limb rotation (Figure 3). Two of the terraces to the south of Pakuashan, P2 and P4, are dated in this study to 19 ± 4 and 19 ± 2 ka, respectively (Table 2 and Appendix C). P2 is most probably younger than P4 because of its lower altitude and gentler tilt: Given the uncertainties, this is consistent with ages obtained using OSL. Also reported along section B-B′ is the top and the strath (surveyed in this study) of the terrace dated by [*Ota et al.*, 2002] to 30,950 ± 290 years B.P., south of the Choushui Hsi (see Figures 2 and 4). Remnants of the lateritic surfaces to the north of Pakuashan, reported along line A-A′, are dated in this study to 21 ± 3 ka (Table 2). (b) North-south projection of profile P5. It shows the typical pattern of imbricate fluvial terraces separated by terrace risers, consistent with the tilt patterns in Figure 5a: Younger terraces appear less tilted and at lower elevations. The location of sample Pakua1-TL, dating terrace P4, is not reported here because it was not collected along line P5.

root into the same level, the Chinshui Shales, at ~4200 m depth.

3.3. Structural Evolution of the Pakuashan Anticline

[14] The Pakuashan anticline has probably developed as a result of thrusting along a decollement within the Chinshui Shales. It probably started as a detachment fold [e.g., *Mitra*, 2003] and is now evolving toward a fault bend fold as a ramp is starting to develop and cut through the detached and folded sections. This structural evolution is typical of fold-and-thrust belts (for other examples, see *Avouac et al.* [1993] or *Shaw et al.* [2002]), and has also been observed in analogue modeling [*Bernard et al.*, 2007].

[15] Deformed fluvial terraces show progressive tilting (Figures 3 and 5) and indicate that some amount of distributed shear (either pure or simple shear) is required. A shear fault bend fold model [e.g., *Suppe et al.*, 2002] is a possibility and has been suggested for the section across southern Pakuashan [*Suppe*, 1983; *Yue et al.*, 2005]. In this case, dips are expected to be constant within dip domains as in the classical case of fault bend folding, although not necessarily parallel to the fault at depth. However, seismic

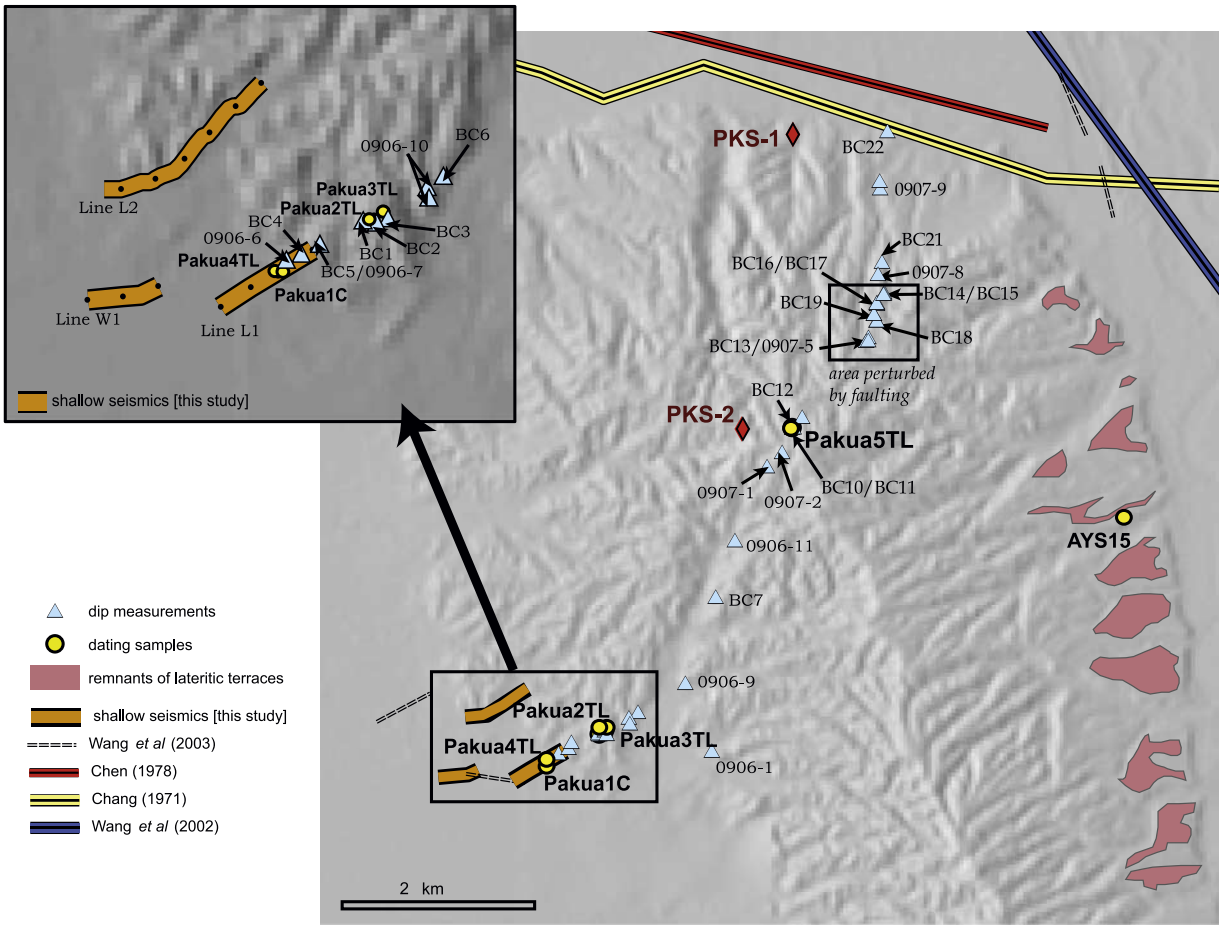

Figure 6. Map of northern Pakuashan (see Figure 2 for location). The location of structural measurements reported in Table 1 is indicated on the map. Age samples (bold characters on map, see Table 2) were mainly collected in the forelimb. Remnants of a lateritic surface, dated to 21 ± 3 ka by AYS15 (Table 2), are also mapped on the 40-m DEM. Shallow seismic investigations have been carried in the westernmost portion of our field area (inset). All these measurements are projected onto line A-A′ (Figure 2).

profiles indicate that in Pakuashan dip angles vary gradually with depth even at the subsurface (Figure 8), excluding the application of this model to Pakuashan. In any case, as explained above, this anticline is best described as a fault tip fold. Because tilted terraces do not provide any evidence for the migration of kink bands (Figure 5) and because together with dips varying with depth they are more consistent with models of distributed pure shear, Pakuashan cannot be considered as a fault propagation fold as defined by *Suppe and Medwedeff* [1990]. Detachment folds [*Dahlstrom*, 1990; *Epard and Groshong*, 1995; *Mitra*, 2003] and trishear fault propagation folds [*Allmendinger*, 1998; *Erslev*, 1991] are examples of models of pure shear fault tip folds. Hereafter we will see that the pure shear fold model proposed by *Bernard et al.* [2007] reconciles both the finite structure and the recent deformation across this anticline.

4. Field Survey and Chronological Constraints on the Stratigraphy

[16] The construction of highway 74 across the northern part of the fold gave us access to fresh outcrops for structural measurements and sampling for the chronology of pregrowth and growth strata across northern Pakuashan (Figures 6 and 7). In southern Pakuashan, we also surveyed a tilted strath terrace (Figures 4 and 5). Tables 1 and 2 summarize the positions, tilts and ages obtained for the different surveyed levels. The topography and the geometry of the preserved lateritic terraces were extracted from the DEM (Figures 4–6).

4.1. Survey of Pregrowth and Growth Strata

[17] The strata along highway 74 across northern Pakuashan are all fluvial deposits from braided to deltaic environments, mostly characterized by fine-grained sandy to argillaceous levels intercalated within poorly sorted coarser-grained sediments (Figure 7). We measured accurately the attitude and position of all the significant strata using a real-time kinematic (RTK) GPS system, coupled to a geodetic laser range distance meter for distant targets. This procedure allows for a very precise relative positioning of the surveyed layers and keeps all measurements tied to a consistent reference frame (procedural details in Appendix B). Theoretically, it is possible to measure the position and

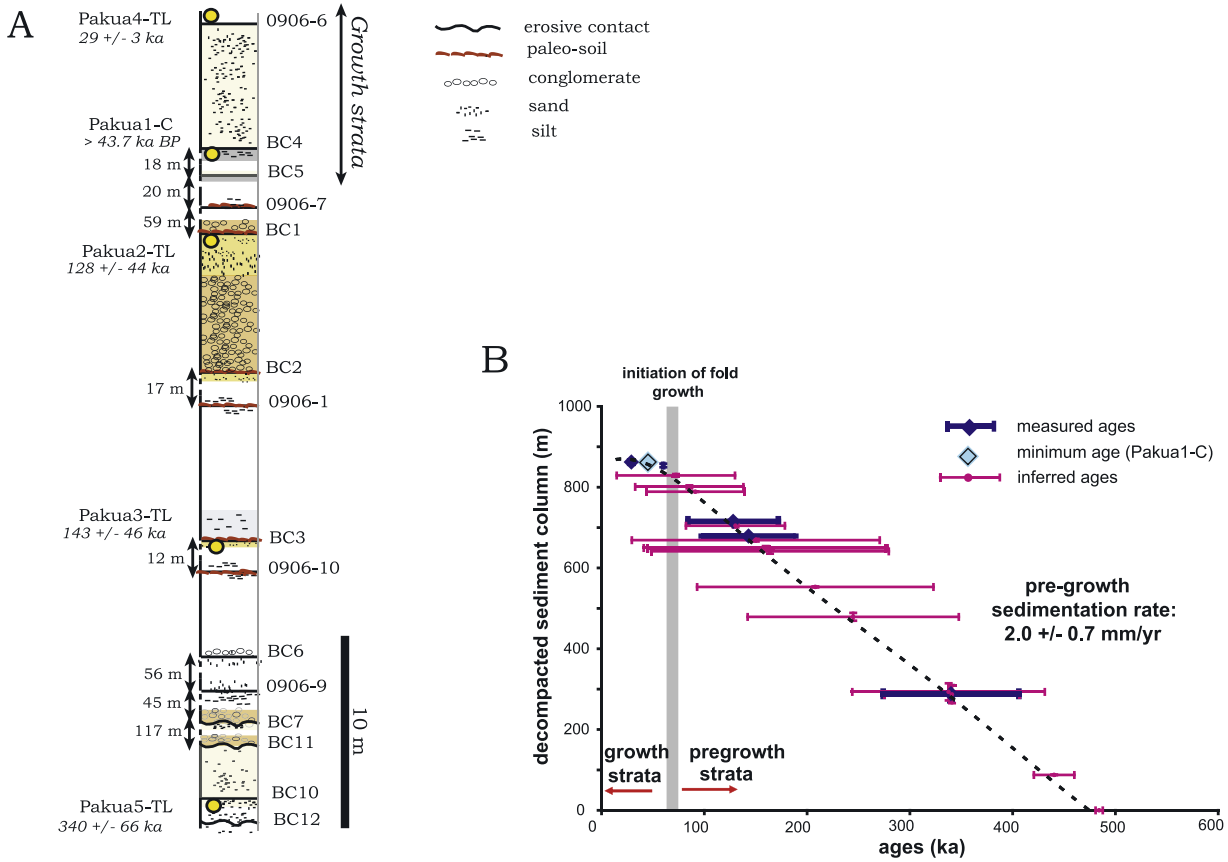

Figure 7. (a) Stratigraphic column of the section surveyed in the forelimb of Pakuashan along highway 74 (northern transect). The position of all samples collected in the field for ^{14}C or OSL dating is reported (Table 2). BC12 is on the axial surface of the fold (Figure 6). (b) Decompacted sediment thicknesses versus depositional ages for all samples from the forelimb of northern Pakuashan. Ages were determined for four samples (blue diamonds). The radiocarbon age of Pakua1-C (light diamond) is only a minimum estimate (Table 2). Other ages (small red circles) are calculated from decompacted sedimentary thicknesses separating samples, pinned to the available OSL age constraints. A weighted least squares regression through all the layers, except those inferred in the field to be growth strata in the frontal zone (Figure 12a), yields a sedimentation rate of 2.0 ± 0.7 mm/yr, indicating that these levels are most probably pregrowth. Given the minimum age from sample Pakua1-C, growth layers at the front yield a much lower sedimentation rate of 0.3 mm/yr at most. See text for details on decompaction of the surveyed units.

orientation of any bed provided that the points measured at the outcrop do not occur on a single line. Often, only an apparent dip angle in the direction of the plane tangent to the outcrop surface can be determined accurately. Apparent dip angles measured along roadcuts were corrected to true dips by considering the azimuth of the fold axis. All these calculations were performed using least squares regressions in which residuals are weighted by the uncertainties on measurements (see Appendix B for details).

[18] We followed essentially contacts between layers with different characteristics, such as contrasted grain sizes (Figure 7). At a number of sites we followed paleosoils defined by thin oxidized levels between adjacent fine-grained deposits. Other markers, such as erosive contacts at the base of river channels filled with conglomerates, were also clearly mapped. Most of the strata observed were moderately to highly weathered. A dark gray argillaceous layer of deltaic sediments was surveyed at the very front of the fold (Figure 12a). Since all strata were deposited in the same environments and since variation of dip angles are subtle (Table 1), it turned out to be difficult to distinguish between pretectonic and syntectonic strata on the basis of our field observations only. Only at one site, subtle progressive unconformities at the very front of the fold suggested the presence of growth strata (Figure 12a). We noticed a N160°E–85°W minor normal fault on the backlimb, which is probably associated with some extrados extension, i.e., extension of the outer surface of the bent layer (Figure 6). This fault may have affected dip angles at sites BC13 to BC17.

[19] To the south, we surveyed the tilted strath surface of a fluvial terrace previously investigated by *Ota et al.* [2002] (Figure 4). Despite the similar sedimentary facies, the strath could be identified from the difference of consolidation between the conglomeratic Toukoshan formation and the less consolidated more recent fluvial deposits on top

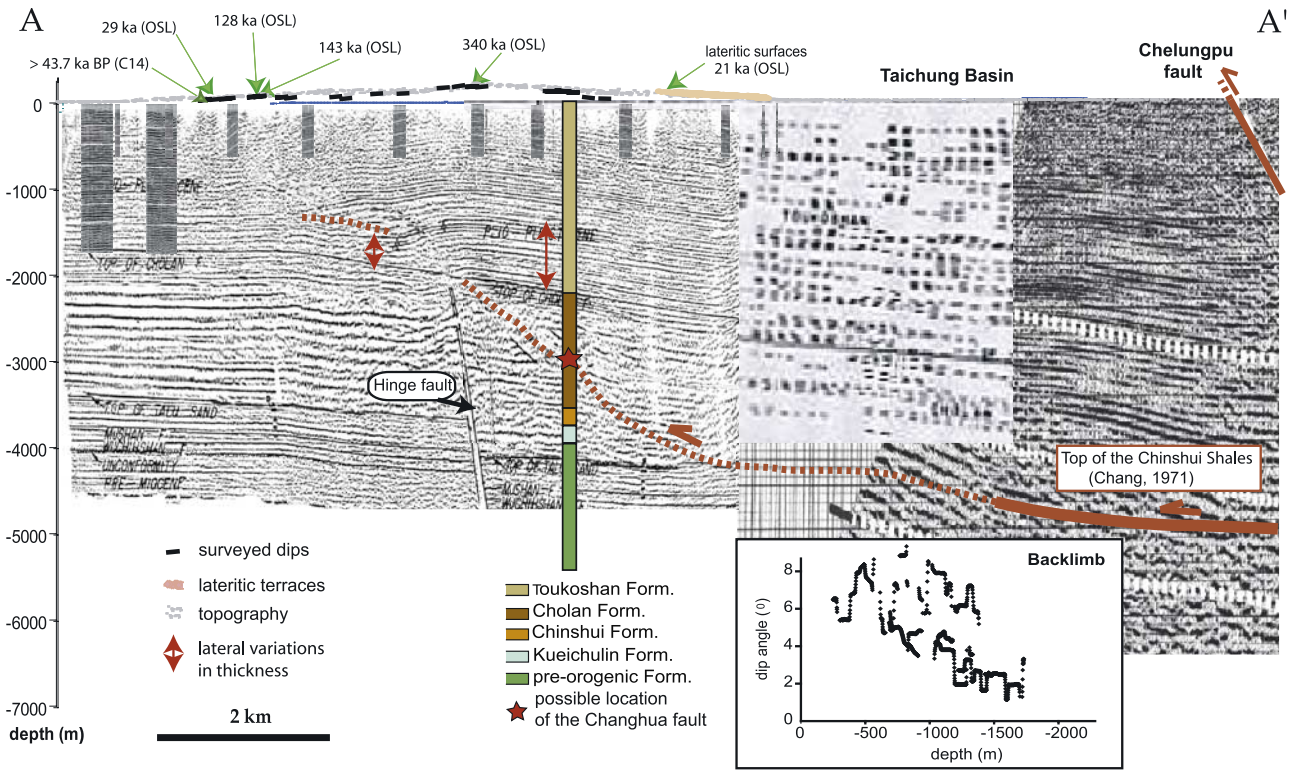

Figure 8. Projection of available data for northern Pakuashan along line A-A′ (Figures 2 and 6). Seismic profiles [*Chang*, 1971; *Chen*, 1978; *Wang et al.*, 2003, 2002] and well logs document the finite structure of the fold. Only the data from the PKS-1 well [*Chang*, 1971] are reported. Because the profile by *Chen* [1978] over most of the Pakuashan anticline has been interpreted in the source paper, some reflectors or discontinuities may be artifacts of this earlier interpretation. The interpreted profile of *Chen* [1978] is reproduced here with traveltimes converted to depths as detailed in Appendix A. The position of the Changhua thrust reported by *Chen* [1978] along the PKS-1 well is indicated (red star). The thick red line locates the top of the Chinshui Shale [*Chang*, 1971], into which the Changhua fault roots. The dashed red line indicates the probable position of the fault that has started to localize. On the profile to the east, the slight flexure of the strata is probably related to the Chelungpu fault. Lateral variations in bed thicknesses at depth (thick red arrows) are evidences for activity of the hinge fault until early Plio-Pleistocene. Inset shows dip angles as a function of depth over the backlimb of Pakuashan. They are calculated point by point along well-defined reflectors. Dip angles increase toward the surface, evidencing deformation by pure shear.

(Figure 12b). This erosive surface appeared to be more tilted than the top of the fluvial deposits (by ~1°) (Figure 5a). Strath terraces are particularly appropriate for morphotectonic analyses because their initial geometry can be compared to the presently active riverbed [e.g., *Lavé and Avouac*, 2000; *Simoes et al.*, 2007].

4.2. Chronological Constraints

[20] Several pieces of wood of more than 100 g each were sampled for radiocarbon dating in the nonoxidized deltaic sediments outcropping at the very front of the anticline along highway 74 (BC4 in Table 2 and Figure 12a). These samples proved to be too old for this method (>43,700 years B.P., Beta-192152). South of the Pakuashan anticline, the tilted strath terrace surveyed in the field (Figure 4) was dated by radiocarbon to 30,400 ± 200 years B.P. (NTU-3279) and 30,950 ± 290 years B.P. (NTU-3509) by *Ota et al.* [2002]. In our analysis, we will consider the older of these two similar ages from *Ota et al.* [2002] since it is most probably closer to the age of riverbed abandonment represented by the strath surface.

[21] Since the outcropping layers are probably too old for radiocarbon and too young and coarse to get good constraints from magnetostratigraphy, OSL dating appeared as the most appropriate technique during our field investigation. This technique dates sediment burial away from sunlight exposure. Principles of the technique and details of the handling of our samples are given in Appendix C. A total of 7 samples were analyzed (Table 2 and Figures 4 and 6). In northern Pakuashan, sample AYS15 dates the remnants of the lateritic surface preserved on the backlimb of the fold (Figure 6). It was collected ~14 m below the top of the terrace, from a weathered fine sandy lens interlayered within coarser gravel. Along Highway 74, Pakua5-TL was collected from the axial line zone, and Pakua2/3/4-TL from the forelimb. Together, these samples span a wide time interval from 21 to 340 ka (Table 2). In southern Pakuashan, AYS16 constrains the age of the lateritic surface P2 to

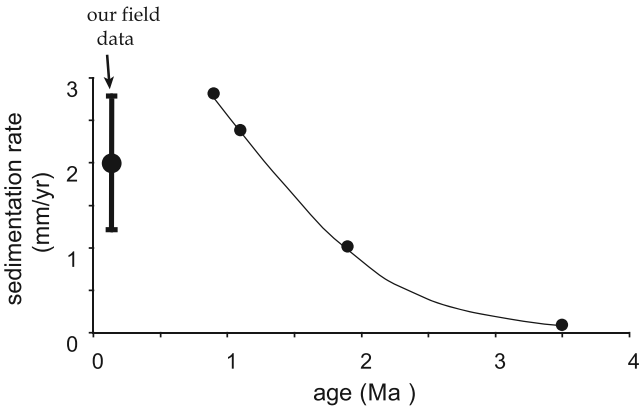

Figure 9. Sedimentation rates derived by decompacting the PKS-1 well log (Figures 2 and 6 for location). Rates of ~2.2 to 2.8 mm/yr over the last million years are similar to the Holocene sedimentation rates measured in the proximal foreland basin [*Lai and Hsieh*, 2003], as well as the 2.0 ± 0.7 mm/yr retrieved from our field measurements in the northern part of Pakuashan (Figure 7).

19 ± 2 ka (Figures 4 and 5 and Table 2). This sample was collected in a trench at a depth of 2.2 m below the surface of the terrace, within a homogenous layer of clay-rich weathered silts overlying well-rounded gravels. Pakua1-TL is taken along a terrace riser, ~30–50 m below the top of the lateritic terrace P4 at this location (Figure 4), and corresponds to fine sandy lenses interlayered within coarser fluvial deposits. This sample is dated to 19 ± 4 ka and probably represents an upper bound for the age of P4. Because deposition rates of fluvial terraces can be quite rapid in this region [*Simoes et al.*, 2007], we attribute this age to the top of P4 in our subsequent analysis. Terrace P2 is certainly younger than P4 because of its gentler tilt and lower altitude (Figure 5). This is consistent with the OSL ages obtained given the uncertainties on the estimates. We did not find any sample to date the other lateritic fluvial terraces represented in Figures 4 and 5. However, the tilt of terrace P1 is similar to the tilt of the terrace dated by radiocarbon to 30,950 ± 290 years B.P. by *Ota et al.* [2002] south of the Choushui Hsi (Figure 5). In the case there is no major lateral variation in the deformation style in the distance between P1 and this terrace, this age can be proposed as a good approximation for P1. No particular constraints are available for P3, except that it should be younger than 19 ± 2 ka (Figure 5).

5. Modeling the Kinematics of the Pakuashan Anticline

5.1. Choice of the Appropriate Model

[22] We aim at determining how cumulative shortening across the Pakuashan anticline evolved over time using depositional ages of pregrowth and growth strata. To retrieve the shortening rate from growth strata [e.g., *Suppe et al.*, 1992] using a graph such as the one in Figure 13, dip

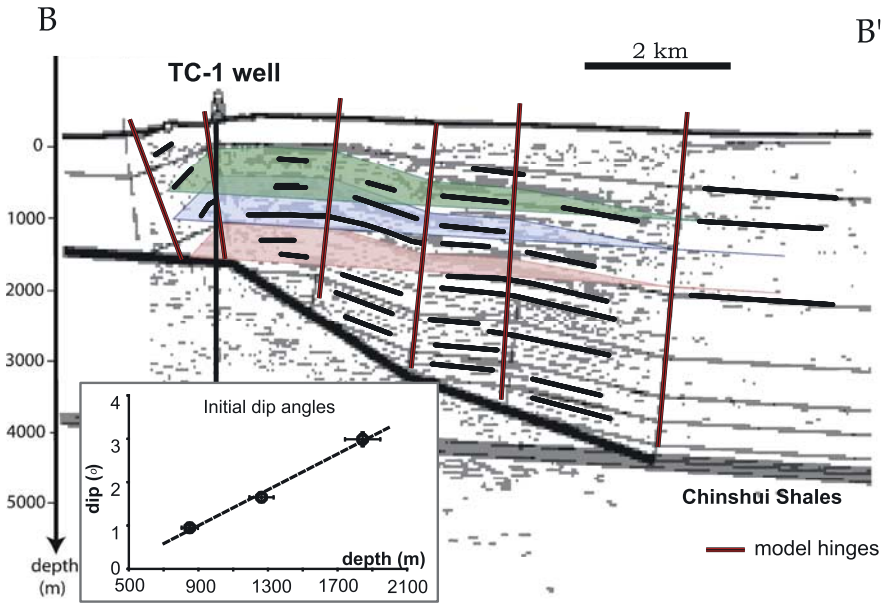

Figure 10. Analysis of the seismic profile for southern Pakuashan [*Hung and Suppe*, 2002] (Figure 4). We did not have access to the original profile and the interpretation by *Yue et al.* [2005] as a shear fault bend fold is shown. In the absence of known deformation west of Pakuashan, we favor an alternative pure shear fault tip fold interpretation (see text for further details). The analysis of this profile is shown as follows: by following reflectors and the general dip trends, three excess area surfaces are extracted to retrieve the finite shortening across the fold. Initial dips of the layers defining the surfaces are extracted from the baselines and vary with depth (inset). See text for further details.

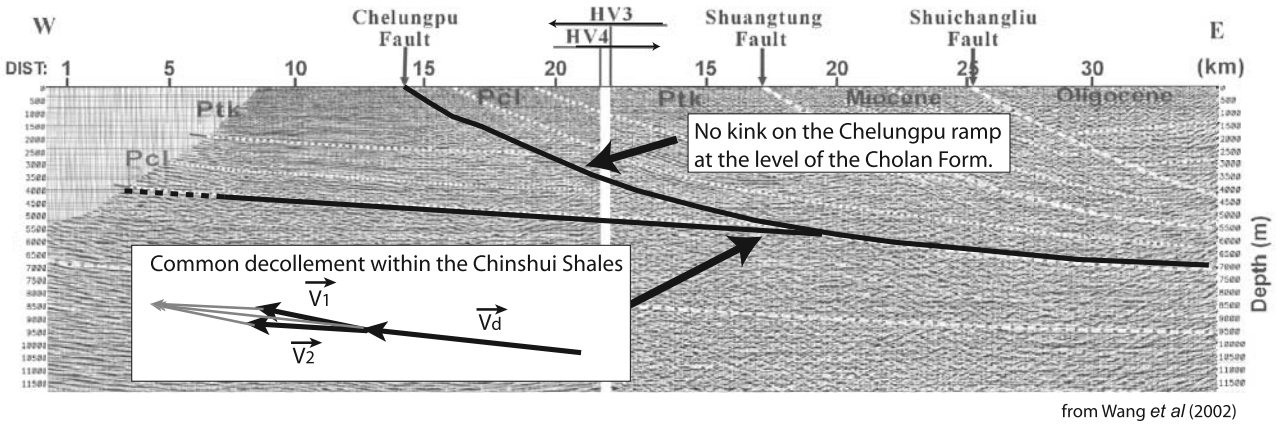

Figure 11. Geometry at the junction between the Chelungpu and the Changhua faults at the level of our northern section, as imaged from the seismic profiles of *Wang et al.* [2002] (Figure 2). Slip $\vec{V}_d$ transferred at depth is partitioned at the junction between the Chelungpu ($\vec{V}_1$) and Changhua ($\vec{V}_2$) faults. If the Changhua fault rooted onto the Cholan formation as proposed by *Chen* [1978], the junction would occur on the ramp of the Chelungpu fault. In this case a kink in the ramp is expected. This is in fact not observed, and the two faults most probably root into the same decollement level within the Chinshui Shales. This is consistent with the observed dip angles of the faults at the junction, if we account for the ~12 to ~15 mm/yr shortening rate on the Chelungpu fault [*Simoes et al.*, 2007], the ~16 mm/yr rate on the Changhua fault derived in this study, and for the subsequent total ~28–31 mm/yr slip rate on the common decollement (vector diagram).

Table 1. Field Measurements for Northern and Southern Pakuashan[a]

Name	Measurement	Longitude	Latitude	Altitude, m	Strike	Dip	2σ on Dip
BC1	RTK	120.56	24.03	75	168	7.0	0.2
BC2	RTK	120.56	24.03	69	168	6.8	0.1
BC3	RTK	120.56	24.03	73	168	5.0	0.1
BC4	RTK	120.55	24.02	31	168	5.1	0.2
BC5	RTK	120.55	24.03	41	168	4.6	0.2
BC6	RTK	120.56	24.03	59	168	6.2	0.3
BC7	RTK	120.57	24.04	105	168	4.1	0.4
BC10	RTK	120.58	24.05	187	168	1.3	0.1
BC11	RTK	120.58	24.05	189	168	2.1	0.1
BC12	RTK	120.58	24.06	186	168	5.5	0.5
BC13	RTK	120.58	24.06	136	168	−1.6	0.1
BC14	RTK	120.59	24.07	122	168	−1.9	0.1
BC15	RTK	120.59	24.07	123	168	−2.0	0.2
BC16	RTK	120.58	24.07	132	168	−6.3	0.8
BC17	RTK	120.58	24.07	132	168	−1.3	0.2
BC18	RTK	120.58	24.06	138	168	−3.5	0.2
BC19	RTK	120.58	24.07	136	168	−3.7	0.2
BC22	RTK	120.59	24.08	49	168	−1.5	0.1
0906-1	laser	120.56	24.03	68	168	7.7	0.6
0906-6	laser	120.55	24.02	36	168	2.0	1.0
0906-7	laser	120.55	24.03	42	168	4.8	0.9
0906-8	laser	120.57	24.04	91	168	5.0	0.5
0906-9	laser	120.56	24.03	57	168	6.1	1.6
0906-10	laser	120.56	24.03	65	168	4.2	1.2
0906-11	laser	120.57	24.04	106	168	2.5	1.5
0907-1	laser	120.57	24.05	175	168	−3.8	3.3
0907-2	laser	120.58	24.05	192	168	8.9	2.7
0907-5	laser	120.58	24.06	131	168	−3.3	1.0
0907-7	laser	120.59	24.07	149	168	−5.3	1.5
0907-8	laser	120.59	24.07	109	168	−3.7	1.5
0907-9	laser	120.58	24.08	82	168	−6.7	0.4
Strath (south)	laser	120.68	23.79	170	90	−2.8	0.2

[a]See Figures 4 and 6. Altitudes are corrected for the observed shift between RTK GPS measurements and DEM data (Appendix B). Apparent dip angles measured on roadcuts are converted to true dip angles by assuming the strike direction. The strath measurement in southern Pakuashan refers to our survey of the strath surface associated with the fluvial terrace dated by *Ota et al.* [2002]. Positive dips indicate plunges to the west, while negative values indicate dips to the east. For further details, see Appendix B.

Table 2. Dating Samples and Associated Surveyed Levels[a]

Site	Sample	Longitude	Latitude	Altitude, m	Method	Age, years
BC4	Pakua1-C	120.55	24.02	31	C14 (Beta-192152)	>43,700 B.P.
-	Pakua1-TL	120.62	23.83	332	OSL	19,000 ± 4,000
BC2	Pakua2-TL	120.56	24.03	69	OSL	128,000 ± 44,000
BC3	Pakua3-TL	120.56	24.03	73	OSL	143,000 ± 46,000
0906-6	Pakua4-TL	120.55	24.02	36	OSL	29,000 ± 3,000
BC10	Pakua5-TL	120.58	24.05	187	OSL	340,000 ± 66,000
-	AYS15	120.61	24.05	68	OSL	21,000 ± 3,000
-	AYS16	120.62	23.89	317	OSL	19,000 ± 2,000

[a]See Table 1 and Figures 2, 4 and 6. OSL analyses were performed at the Planetary and Geosciences Division of the Physical Research Laboratory (Ahmedabad, India). Pakua1-TL and AYS16, in the southern section of the anticline, date the lateritic surfaces P4 and P2, respectively (Figure 4). The remnants of the lateritic surface to the north are dated by AYS15 (Figure 6). See Appendix C for details on the handling of the samples.

angles measured in the field are to be converted into cumulative shortening. For that a model of fold growth is needed.

[23] As discussed previously, there is convincing evidence that the Pakuashan anticline is a fault tip fold with limb rotation resulting from pure shear (Figures 3 and 5). Numerous pure shear fold models have been described in

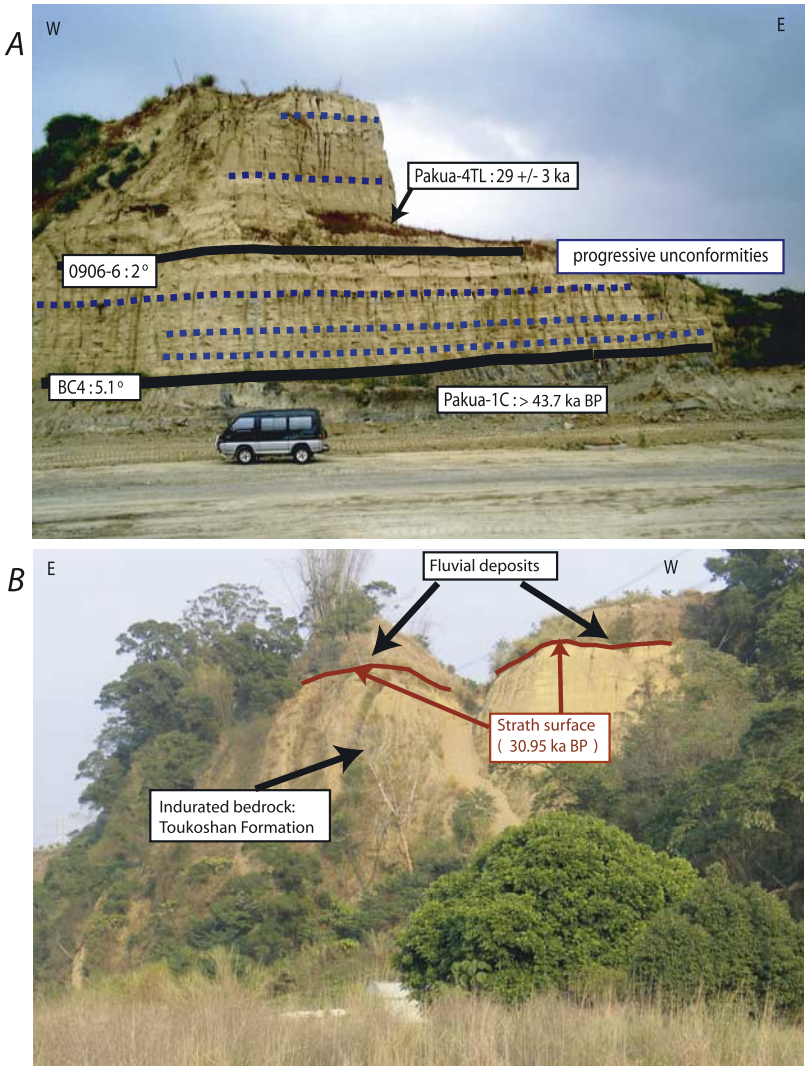

Figure 12. Pictures of the field survey. (a) Field picture locating BC4 and 0906-6 sedimentary contacts (black lines) and dating samples Pakua4-TL and Pakua1-C in northern Pakuashan (Figure 6 and Tables 1 and 2). Also emphasized in this picture are the dips of successive sediment layers (blue dotted lines), showing subtle progressive unconformities. (b) Strath surface associated to the 30,950 ± 290 years old terrace [*Ota et al.*, 2002] south of the Pakuashan anticline (Figure 4). This erosive contact separates the more indurated fluvial sediments of the Toukoshan Formation and the more recent deposits that were sampled for dating.

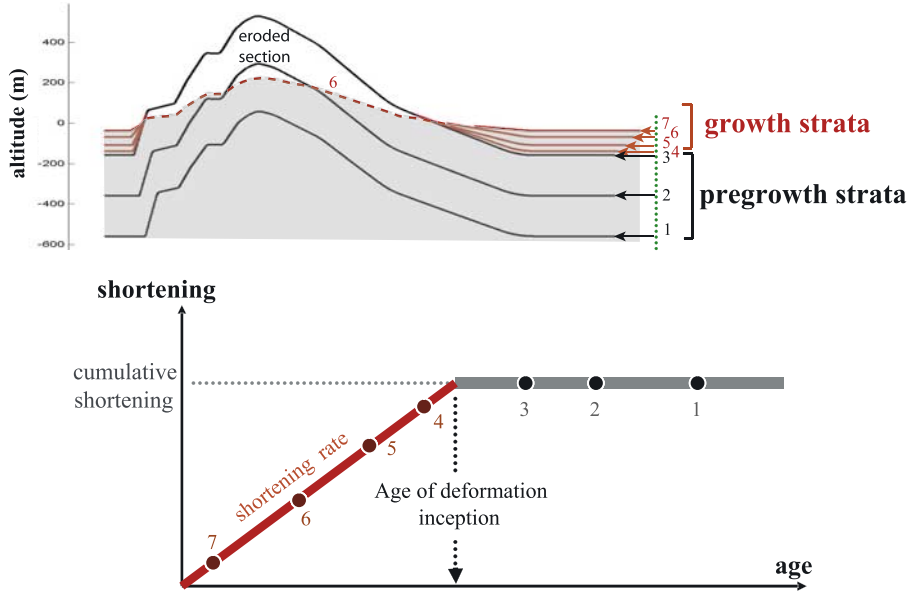

Figure 13. Schematic deformation pattern of a fault tip fold and principle of our approach. Strata deposited prior to fold growth (black) have all recorded the same amount of cumulative shortening. Younger growth strata (red), which were deposited during fold growth, have recorded different increments of shortening [e.g., *Suppe et al.*, 1992]. The shortening rate, here assumed constant, and age of folding inception can be determined from such a plot.

the literature. These include the detachment fold model [*Dahlstrom*, 1990; *Epard and Groshong*, 1995; *Mitra*, 2003] or the trishear fault propagation fold model [*Allmendinger*, 1998; *Allmendinger and Shaw*, 2000; *Erslev*, 1991; *Zehnder and Allmendinger*, 2000]. The high competence contrast between sedimentary units, usually invoked for detachment folds, is not observed in the present case. For the trishear approach, an unlimited number of velocity fields can be generated by varying the propagation-to-slip ratio of the fault [*Allmendinger*, 1998; *Allmendinger and*

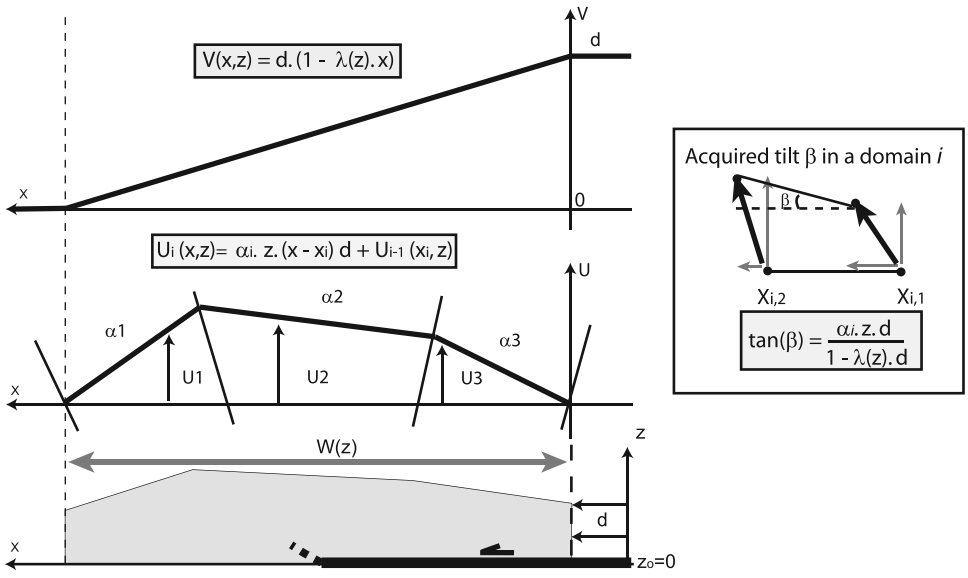

Figure 14. Sketch illustrating how (top) horizontal displacements and (middle) uplift relate to incremental shortening d according to the pure shear fold model of *Bernard et al.* [2007], as expressed by equations (1) and (2). Inset illustrates how the dip angle β acquired in a dip domain i relates to the incremental shortening d as a function of the model parameters (α_i and λ) and of elevation above the decollement z as expressed by equation (3).

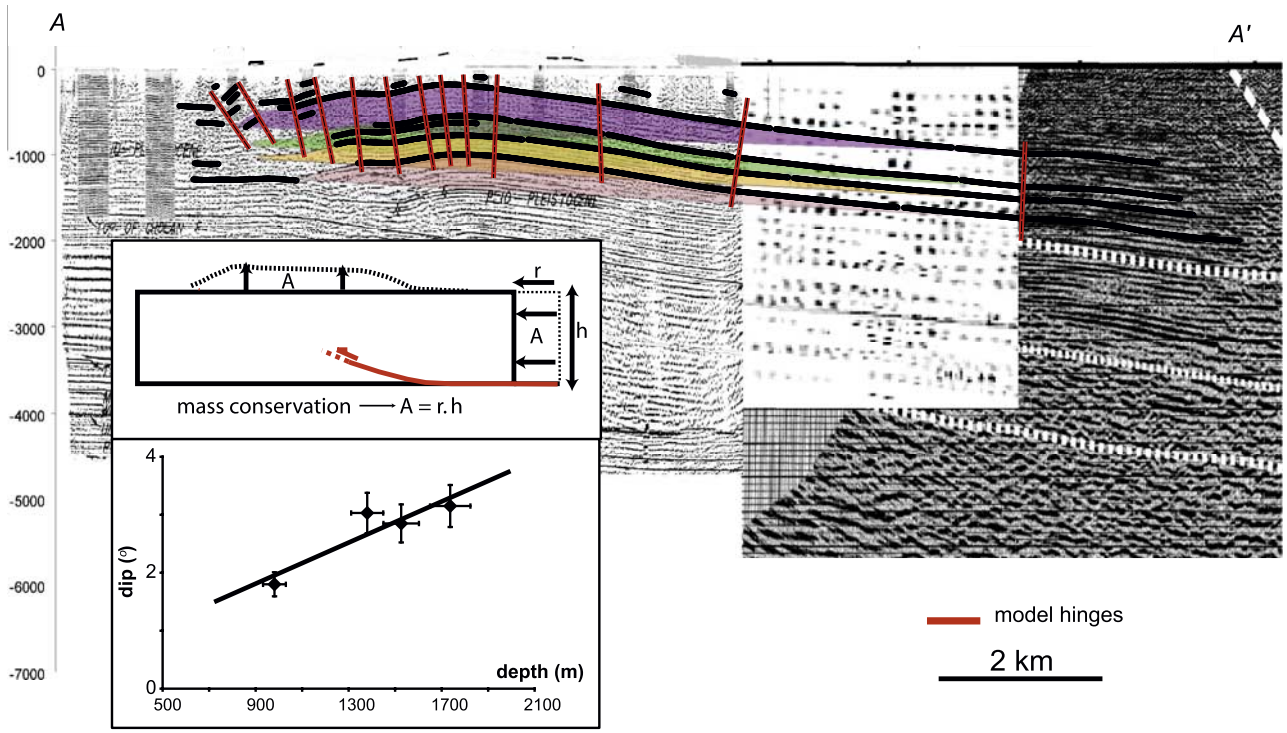

Figure 15. Analysis of the seismic profiles for northern Pakuashan, projected onto section A-A′ (Figure 2). Only the shallow levels not affected by the buried hinge fault (Figure 8) are digitized and modeled. Colored surfaces show the excess area defined by the major reflectors that can be traced over most of the fold. Mass conservation implies that excess area is proportional to cumulative shortening and to the height of the reflectors above the decollement (equation (5), top inset). The baselines of the surfaces represent the probable initial geometry of the reflectors. They show a dip angle increasing with depth (bottom inset). Red lines indicate the axial surfaces delimiting the dip domains considered in the modeling.

Shaw, 2000; *Zehnder and Allmendinger*, 2000], for which we do not have any geological constraints in the case of the Changhua fault. Finally, these models would in principle apply to Pakuashan but we did not find any simple way of using them in a parameterized form that would make it possible to adjust accurately the observed structure of this anticline. We therefore favor an alternative approach based on the fold model of *Bernard et al.* [2007], which is derived from a sandbox experiment composed of sand layers intercalated with glass beads. Given the cohesion of these materials, the sand thickness of 4.8 cm is equivalent in nature to 4.8 km of sediments. In this experiment, a fault tip fold develops at the front of a critical sand wedge, which mimics a fold-and-thrust belt system at the back of the growing frontal fold. Given the boundary conditions, the probable material properties and the scaling factor, the experiment is an appropriate analogue to a fold such as Pakuashan. During fault tip folding, *Bernard et al.* [2007] observe that internal deformation occurs by distributed pure shear until a ramp forms by strain localization. From the displacement field monitored by a video system, *Bernard et al.* [2007] propose simple analytical expressions for incremental horizontal and vertical velocity fields (Figure 14). In practice, any model assuming mass conservation (as this one does) should yield the same shortening history provided that continuous deformed layers can be retrieved across the whole fold. However, for Pakuashan, only discontinuous markers of deformation were surveyed in the field. The model derived by *Bernard et al.* [2007] has the capacity to deal with such discontinuous markers, and is actually simpler to implement than other existing models. This study is the first application of this model to a natural setting.

5.2. Analytical Expressions for Incremental Displacements and Tilting During Folding

[24] The key observation in the sandbox experiment of *Bernard et al.* [2007] is that the horizontal velocity varies linearly over the whole fold area and that the uplift rate varies linearly within domains separated by axial surfaces. These axial surfaces remain approximately fixed relative to the undeformed footwall (Figure 14). The incremental horizontal displacement $v(x, z)$ resulting from an increment of shortening d at the back of the thrust sheet is a linear function of distance x between the first and last hinges of the fold (Figure 14):

$$v(x,z) = d(1 - \lambda(z)x) \tag{1}$$

where z is the elevation above the decollement level, and $\lambda(z) = 1/W(z)$ with $W(z)$ the width of the fold at elevation z.

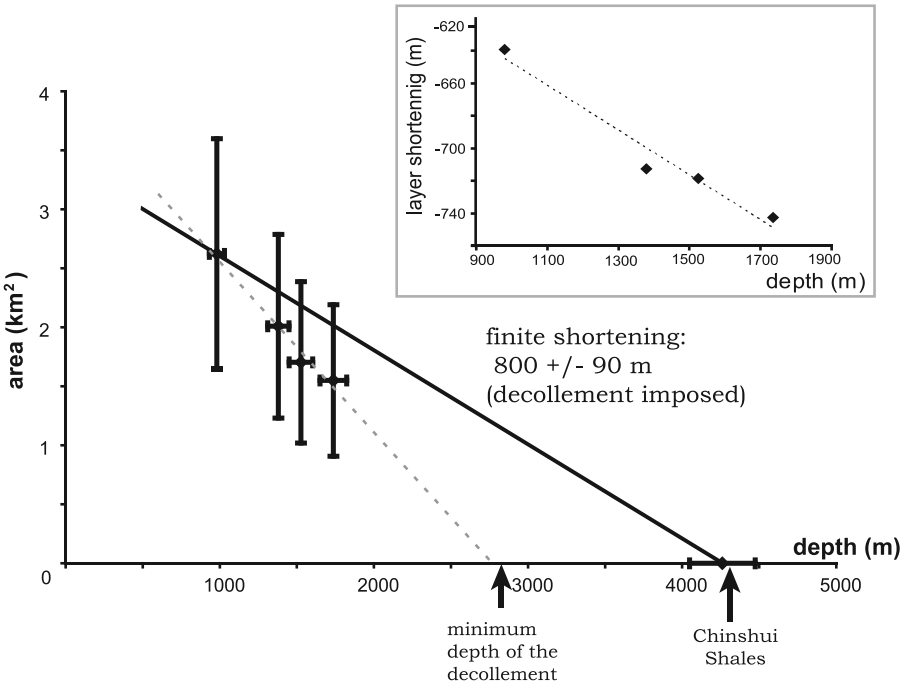

Figure 16. Excess area as defined in Figure 15 versus depth for section A-A′ across northern Pakuashan. A weighted least squares regression favors a 2770 ± 2300 m decollement depth and a finite shortening of 1440 ± 780 m (dashed line). To reduce uncertainties on these values, the decollement is imposed within the Chinshui Shales, as indicated from independent data. In this case, the retrieved finite shortening is 800 ± 90 m. The minimum depth of the Changhua decollement is given by the evidence of a fault zone along the PKS-1 well [*Chen*, 1978] (Figure 8). Inset shows layer shortening versus initial depth. It is calculated by comparing total shortening retrieved from the line length method and the value of 800 m obtained from the excess area technique.

Incremental vertical displacement $u_i(x, z)$ is also a linear function of horizontal distance within each domain i defined by two consecutive axial surfaces:

$$u_i(x,z) = \alpha_i z d(x - x_i) + u_{i-1}(x_i, z) \tag{2}$$

where α_i is a parameter characteristic of domain i (Figure 14), and x_i is the horizontal position of the axial line separating consecutive domains i and $i - 1$. The term $u_{i-1}(x_i, z)$ is the incremental uplift at the point of coordinate (x_i, z) along the axial line, and ensures continuity of vertical displacements between consecutive domains. Deformation by distributed pure shear allows for limb rotation during folding. Within the domain i, the change in dip angle β_i associated with an incremental shortening d is given by

$$\tan(\beta_i) = \frac{\alpha_i z d}{1 - \lambda(z)d} \tag{3}$$

from equations (1) and (2) (Figure 14). Equation (3) can be simply used to convert the dip angle of a pregrowth or growth stratum into cumulative shortening. Equations (1)–(3) provide an Eulerian description of the velocity field that should be used only for infinitesimal incremental deformation.

[25] Another approach consists in comparing dip angles of growth and pregrowth strata at the same location (x, z). In domain i, strata with different dips $\beta_{i,1}$ and $\beta_{i,2}$ and originally at the same altitude z have different cumulative shortenings, d_1 and d_2, respectively. If d_1 is known, as for pregrowth layers (in this case $d_1 = D$ where D is the total cumulative shortening), then d_2 can be estimated:

$$d_2 = \frac{\tan(\beta_{i,2}) d_1}{\tan(\beta_{i,1})(1 - \lambda(z)d_1) + \tan(\beta_{i,2})\lambda(z)d_1} \tag{4}$$

This formulation does not depend on the parameter α_i, which is more sensitive to the seismic profile resolution than $\lambda(z)$. It should be noticed that equations (3) and (4) only apply to domains where dip angles are not subhorizontal. In the case dip angles are close to being horizontal, and provided that the initial burial depth is known, an alternative approach is to calculate cumulative shortening from the total uplift of the layer using equation (2), or, equivalently, from the amount of shortening needed to retrodeform the layer back to its assumed initial position. This approach applies essentially to layers that can be traced continuously across the fold zone.

5.3. Fold Model for Northern Pakuashan

[26] The analytical model is calibrated from the modeling of the finite deformation as revealed by the deep structure of the Pakuashan anticline. We follow the procedure proposed by *Bernard et al.* [2007].

5.3.1. Calibrating Model Parameters From Seismic Profiles

[27] Well-defined reflectors that can be traced across a significant fraction of the fold are first selected (Figure 15).

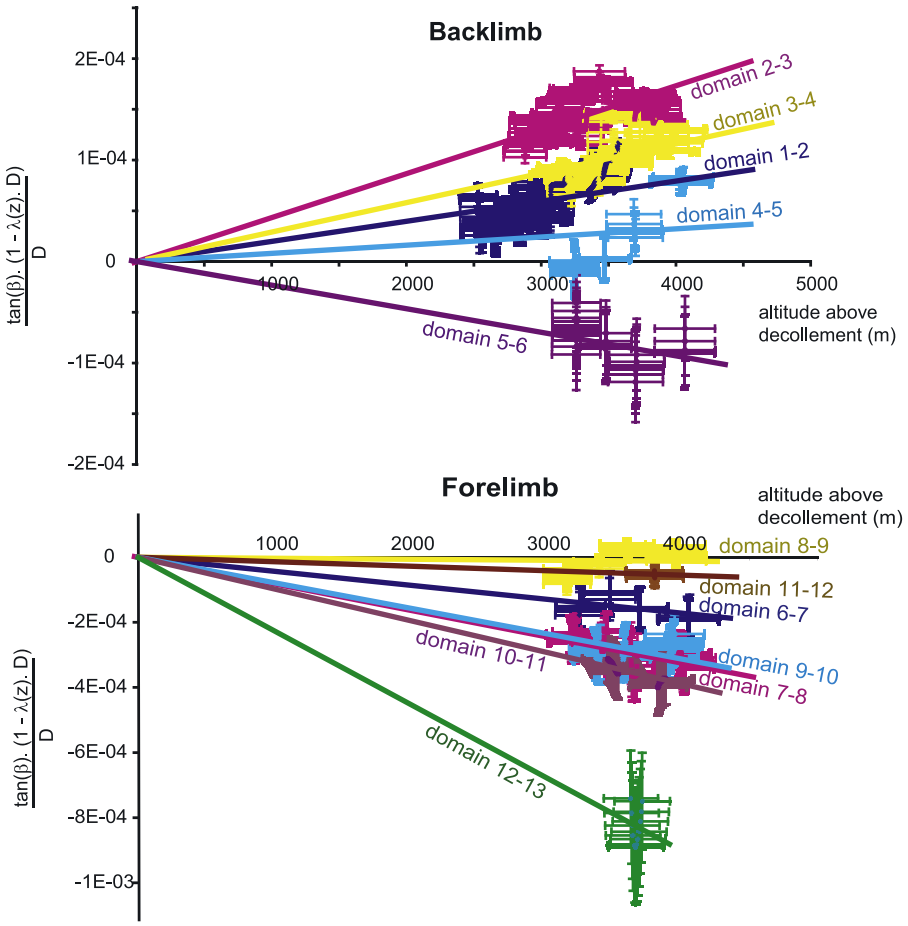

Figure 17. Plot of $[\tan(\beta_i)(1 - \lambda(z)D)]/D$ as a function of the altitude z of a layer above the decollement, for dip domains (top) within the backlimb and (bottom) within the forelimb of northern Pakuashan. Numbers identifying dip domains relate to the axial surfaces delimiting them. The first axial surface is taken at the back of the fold and numbers increase from east to west (Figure 15). For instance, the first two axial surfaces to the east define domain 1–2. Dips β are calculated along the reflectors digitized on the seismic profiles (Figure 15). Several data points are considered for each domain. The altitude z corresponds to the initial altitude of the reflector, prior to deformation, as estimated from the baselines of the excess area surfaces. Calculation of uncertainties is detailed in Appendix D.

The strata below ~1500–2000 m, which are affected by the buried hinge fault (Figure 8), are discarded. We select four reflectors that are conformable and most probably predate initiation of shortening on the Changhua fault (Figure 15). The baseline obtained by linearly interpolating the extremity of these reflectors is interpreted to represent the initial geometry of the layers. The dip angle of this baseline increases linearly with depth (bottom inset in Figure 15). This is consistent with the development of the flexural basin that predates deformation, and compaction of the sediments may have amplified the pattern. Total shortening is estimated from the excess area method [*Epard and Groshong*, 1993]. If folding results from a total horizontal shortening D of a unit with thickness h detached from the footwall, mass conservation implies that the area A above the baseline is:

$$A = D \quad h = D(Z - Z_d) \tag{5}$$

where Z and Z_d are the depths of the baseline and of the decollement, respectively (top inset in Figure 15). Equation (5) assumes that cross-sectional area is preserved during folding, implying that out-of-the-plane transport and volume changes can be neglected. Using this approach, a regression with account on the uncertainties on the depths and on the areas (Appendix D) yields a decollement depth of 2770 ± 2300 m and a total cumulative shortening of 1440 ± 780 m (Figure 16). In the absence of independent constraints on the decollement depth, these results favor a decollement within the Cholan formation. The large uncertainty is however compatible with a decollement within the Chinshui Shales, which seems more plausible as discussed earlier (Figure 11). Accordingly, if we impose the decollement to lie within the Chinshui shales at a depth of 4200 ± 860 m, the shortening is then estimated to 800 ± 90 m (Figure 16). From this value, we also calculate line length changes and find that beds have shortened by ~−640 to −742 m (Figure 16). This is a significant amount relative to the total shortening across the fold, and confirms that the Pakuashan anticline has formed primarily by distributed pure shear.

Table 3. Model Parameters for Northern Pakuashan[a]

Parameters	Values	Uncertainties
Total shortening, m	800	90
λ (at surface)	−9.50E-05[b]	2.48E-06
α		
Domain 1–2	2.22E-08	1.23E-10
Domain 2–3	4.35E-08	1.30E-10
Domain 3–4	2.78E-08	2.94E-10
Domain 4–5	1.37E-08	3.93E-10
Domain 5–6	−2.27E-08	1.43E-09
Domain 6–7	−4.17E-08	1.81E-09
Domain 7–8	−7.98E-08	2.04E-09
Domain 8–9	1.24E−09	7.49E−10
Domain 9–10	−7.76E-08	2.52E-09
Domain 10–11	−9.68E-08	3.19E-09
Domain 11–12	−1.36E-08	2.98E-09
Domain 12–13	−2.24E-07	1.33E-08

[a]Uncertainty calculations are detailed in Appendix D. Numbers identifying dip domains relate to the axial surfaces delimiting them. The first axial surface is taken at the back of the fold and numbers increase from east to west (Figure 15). For instance, the first two axial surfaces to the east define domain 1–2.

[b]Read −9.50E-05 as -9.50×10^{-5}.

[28] Model parameters are then calibrated. Dip angles are calculated from point to point along these reflectors. We next define 12 dip domains across the fold (Figure 15). This number is somewhat arbitrary and was found, by trial and error, to provide a reasonable representation of the anticline. The parameter $\lambda(z)$ is determined from the fold width $W(z)$, which is calculated from the distance between the first and the last axial surfaces. In the first-order approximation that equation (3) holds for finite dip angles, the dip angles observed in the seismic profile and the total shortening D across northern Pakuashan can be used to estimate the parameters α_i for each dip domain. In Figure 17, we plot $[\tan(\beta_i)(1 - \lambda(z)D)]/D$ (where D is 800 ± 90 m) as a function of the initial altitude z above the decollement as estimated from the baselines of the surfaces in Figure 15. Equation (3) suggests that this should be a linear relation, with α_i being the slope. The observed linear trend indicates the consistency of the model with the data. The values of α_i and related uncertainties (Table 3) are calculated from a weighted least squares regression (Appendix D).

5.3.2. Modeling Cumulative Deformation

[29] We check here that the calibrated model reproduces well the observed fold geometry. We compute incremental fold growth, with increments of shortening of 10 m, up to a total shortening D of 800 ± 90 m, and we find that predicted and observed finite geometries are in good agreement (Figure 18a). At each point, predicted and observed dip angles are compared. The mean residual is 0.1° and the standard deviation of this residual is 3°. Most of the misfit occurs along axial lines and in the frontal most area of the fold where the model does not adequately reproduce the steep dip angles, as observed from shallow seismics (Figure 8). The misfits are thus not biased and are of the order of the uncertainty on observed dips. This misfit provides an estimate of the error associated with the calibrated model. The model can also be used to restore incrementally the layers digitized from the seismic profiles (Figure 18b). The horizons selected on Figure 15 are restored to linear horizons with shallow dip angles consistent with those retrieved from the baselines in Figure 15.

5.4. Fold Model for Southern Pakuashan

[30] In the case of southern Pakuashan, we follow the same approach as for the northern transect based on the seismic profile of *Hung and Suppe* [2002], as interpreted by *Yue et al.* [2005] (Figure 10). The precision is not as good as for northern Pakuashan, in particular at the front of the fold where some reflectors suggest layers dipping steeply to the west. Domains of homogeneous dip angles are determined. The excess area method yields a total shortening D of 850 ± 90 m if we fix the depth of the decollement to ~4200 m within the Chinshui Shales (Figure 19). Initial dip angles as defined from the baselines (Figure 10), and parameters $\lambda(z)$ and α_i are retrieved from the seismic profile (Table 4). Here also, the linear relation observed between $[\tan(\beta_i)(1 - \lambda(z)D)]/D$ and the altitude z above the decollement (Figure 20) illustrates the consistency between the model and the actual mode of folding. The reconstructed fold geometry matches well the observed pattern, except for the frontal most area. The fit to the data is here not as good as for the northern transect, due possibly to the poorer quality of the interpreted seismic profile (Figure 10). The mean residual between observed and predicted dip angles is 0.6°. The standard deviation of this misfit is 4.8°, and drops to 3.5° if the frontal area is not included. This latter value is subsequently considered (Appendix D) because our field measurements in this area are all on the backlimb of the fold.

5.5. Determination of the Shortening History

[31] Dip angles measured in the field are first corrected for the estimated initial geometry of the layer. The estimated tilts are then converted into shortening using equations (3) or (4).

5.5.1. Analysis of Southern Pakuashan

[32] We use here the tilt recorded by three dated geomorphic markers: the strath terrace dated to 30,950 ± 290 years B.P. [*Ota et al.*, 2002], and lateritic surfaces P2 and P4 (Figure 4) dated to 19,000 ± 2000 years and 19,000 ± 4000 years, respectively (Table 2). The initial geometry of the strath terrace can be approximated by the present gradient of the Choushui Hsi (0.4°W). More precisely, because of the wide distribution of ancient fluvial terraces in the area, it can be expected that the fluvial valley was wider in the past so that the river gradient was less steep than at present. Given this possibility, we consider a wide range of possible initial dip angles for the strath of 0.2 ± 0.2°W. We measure on the DEM average values of 1.7 and 2.2°E dip angles for P2 and P4, respectively (Figure 5a). These values are taken over most of the backlimb of the fold. They do not include the highest and lowest portions of P2 and P4 where the terraces may not be sampled because of hillslope processes, or sedimentation at the back of the fold. Assessing the initial geometry of these surfaces is non trivial, and we were not able to identify in the field the bottom of the fill deposits. To account for this unknown, we therefore use in our analysis the tilt measured from the top of the terraces and assign a large uncertainty of 1°.

[33] Using the calibrated fold model, we calculate the dip angles predicted for pregrowth strata at the location of these

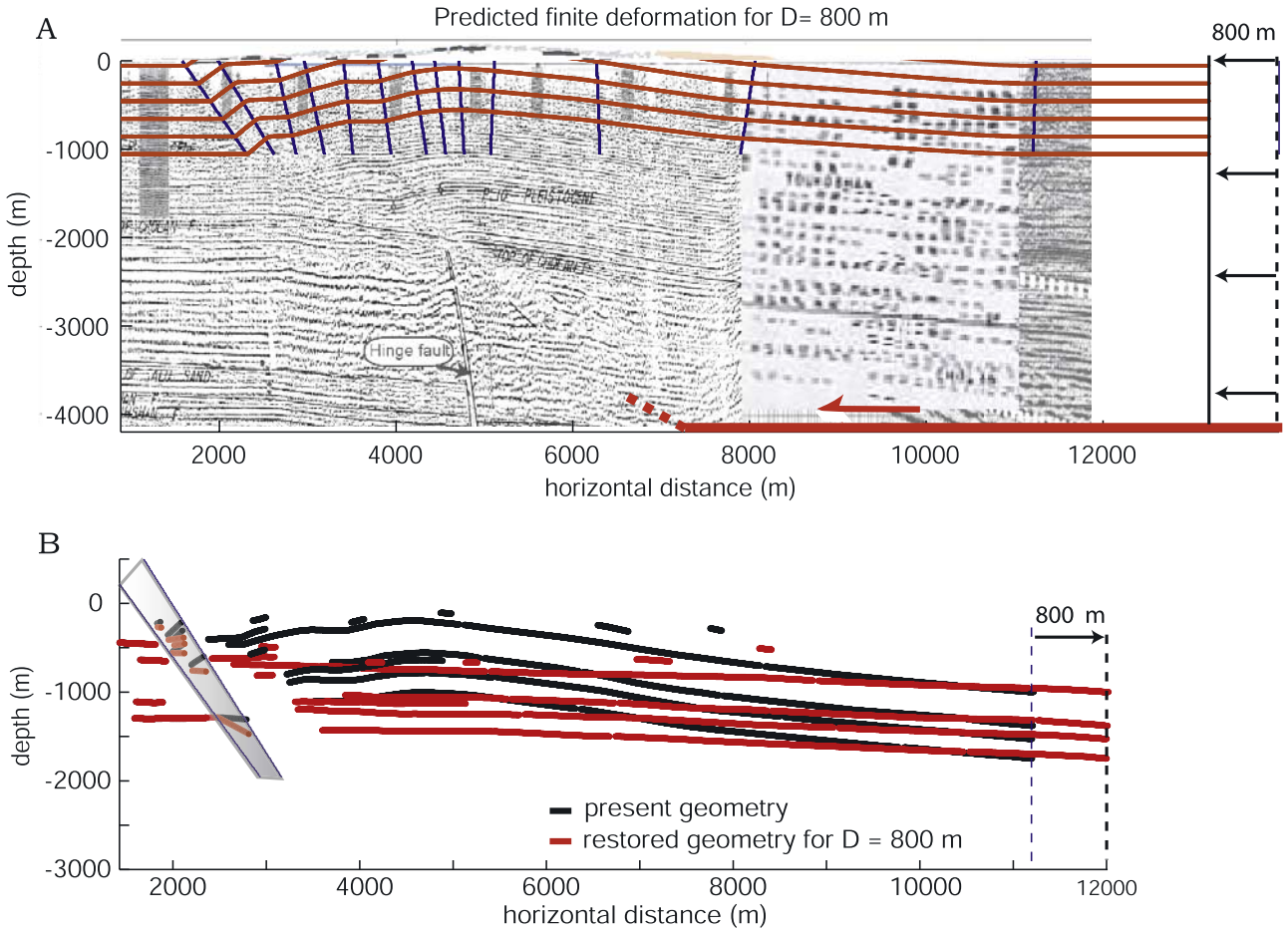

Figure 18. Modeling finite deformation from the calibrated fold model for northern Pakuashan. Model parameters are listed in Table 3. (a) Predicted deformation for initially horizontal levels (red lines) after 800 m of total shortening. This pattern is compared to the seismic profile of Figure 8. The geometry of the blind thrust is schematic and only indicates the depth of the decollement. The misfit between the observed and predicted dips is 0.1° on average. The standard deviation of the distribution of the misfit is of 3° and is used to estimate the error on the predicted dip angles using the calibrated fold model. (b) Restored geometry of the reflectors indicated in Figure 15. The restoration is based on the calibrated fold model for 800 m of shortening. The original geometry inferred from this analysis predicts initial dip angles that range from 2.1° to 1.8°, in good agreement with data. The misfit between model and observations is largest at the front of the fold (shaded area). The deepest level in this shaded area shows a predicted initial dip angle too steep because this level does not seem deformed in the original seismic profile.

geomorphic markers, and subsequently use equation (4) to derive the cumulative shortening of these terraces. These values and the ages of the terraces provide a shortening rate of 15.2 ± 3.7 mm/yr across southern Pakuashan (N90 ± 5 E direction). Since the finite shortening across the fold in this area is of 850 ± 90 m, deformation would have initiated 55,700 ± 6300 years ago (the procedure used to estimate uncertainties is detailed in Appendices E and F). From the tilt of the lateritic terraces P1 (3.9°E) and P3 (1.5°E) (Figure 5), we estimate their cumulative shortenings to ∼580 and ∼240 m, respectively. The shortening rate derived for southern Pakuashan suggests that terraces P1 and P2 would be ∼38,100 and ∼15,700 years old, respectively.

5.5.2. Analysis of Northern Pakuashan

[34] In this section, we consider our field data along highway 74 (Table 1), which may encompass both pregrowth and growth layers. In the case of the pregrowth layers, the relation between depositional depth and initial dip angle obtained in Figure 15 is used to correct our structural measurements and estimate tilts acquired during folding. We can not simply assess the initial geometry of the growth strata, and we therefore assign them a large uncertainty of 1°.

[35] Because subtle dip changes did not permit clear identification of pregrowth from growth strata in the field, we differentiate them on the basis of the sedimentation rate estimated from the stratigraphic thickness separating the dated samples (Figure 7). Indeed, we expect sedimentation rates of 2 to 3 mm/yr in the case of strata deposited before deformation inception, as inferred from PKS-1 (Figure 9), and lower values for growth layers. As along highway 74 all OSL ages were obtained on samples from the forelimb, and

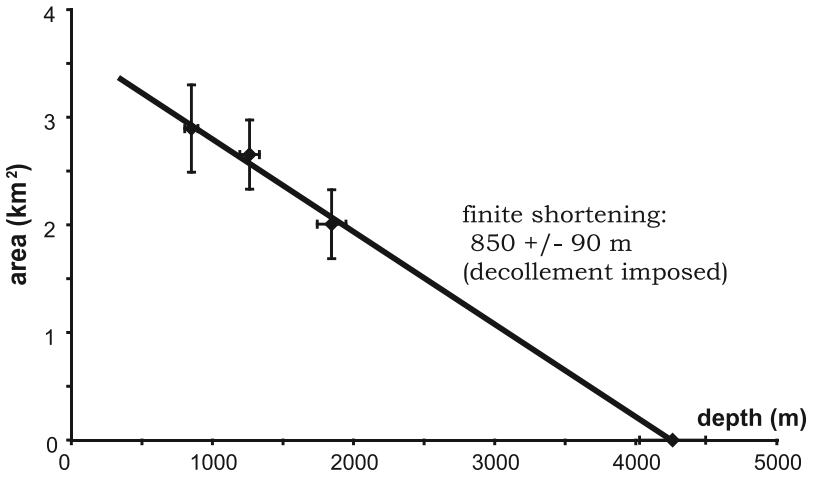

Figure 19. Excess area analysis of the section across southern Pakuashan. A finite shortening of 850 ± 90 m is found when the decollement is imposed to lie within the Chinshui shales. This plot does not show evidence for backshear, in contrast with *Suppe*'s [1983] and *Yue et al.*'s [2005] interpretations.

as some faulting was observed on the backlimb, only the data from the forelimb are considered here. To estimate the sedimentation rates from stratigraphic thicknesses, sediments are decompacted using the porosity-depth law of *Audet* [1995] and the parameters determined by *Lin et al.* [2003] from the BD1 well offshore western Taiwan. To solve for the burial depth of the units, we assume first that BC12, along the axial zone (Figure 6), is pretectonic. We use the fold model calibrated previously to retrodeform BC12 by ~800 m. This calculation implies an initial depth of ~418 m. Using this value, initial burial depths for other data points are estimated, and decompacted sedimentation rates are calculated (Figure 7b). A weighted linear regression through all the data yields a rate of 1.5 ± 0.2 mm/yr, too low in view of the constraints from PKS-1 (Figure 9). If the layers inferred to be syntectonic at the front of the fold because of observed progressive unconformities (Figure 12a) are discarded, we get a sedimentation rate of 2.0 ± 0.7 mm/yr (Figure 7b) in reasonable agreement with the rate inferred from PKS-1 (Figure 9). This indicates that all the strata surveyed in the field are pregrowth except for those in the frontal most portion of the anticline. From the sedimentation rate pattern of Figure 7b, the transition between pregrowth and growth strata indicates that folding initiated ~70 kyr ago.

[36] We then correct measured dip angles for the assumed initial geometry. In the case of the surveyed pregrowth layers, corrected dip angles do not vary much in the forelimb, with an average value of 6.1 ± 1.7°W consistent on a first approximation with the fold model derived along the Tatu Hsi river (Figure 21). This value certainly holds further west as indicated by the shallow seismic line L1 (Figure 21). Slightly further north (Figure 6), steeper angles of ~10–12°W are shown on the easternmost portion of line L2. This suggests that there are significant lateral variations in the geometry of the structures over northern Pakuashan. Therefore we will only rely on the geometry of surveyed pregrowth strata and on line L1, which was shot along highway 74 (Figure 6). To simplify our analysis with equation (4), we therefore assume a value of 6.1 ± 1.7°W for the dip angles of pregrowth strata over the section surveyed in the forelimb.

[37] Finally, we use equation (4) to estimate the cumulative shortening of layers surveyed along highway 74 and of the tilted lateritic terraces dated by AYS15 on the backlimb (Figure 6). Most strata yield a cumulative shortening consistent with the 800 ± 90 m total shortening inferred from the excess area technique except for the growth strata dated to 29,000 ± 3,000 years and for the lateritic surfaces dated to 21,000 ± 3000 years (Table 5). Use of these data alone yields a shortening rate of ~10.7 mm/yr. With a total shortening of ~800 m, it indicates an age of folding inception of ~74,700 years, slightly too old in view of the youngest pregrowth layer derived in Figure 7. This tendency is essentially related to the growth layer surveyed in the forelimb (Figure 22). When we also account for the youngest pregrowth layer as giving the minimum age of initiation of deformation, we get a shortening rate of 11.2 ± 1.8 mm/yr (along section A-A′, Figure 2) and an age of folding inception of 71,300 ± 8,100 years.

5.6. Kinematics of the Pakuashan Anticline: Shortening Rate and Age of Deformation Inception

[38] When data from southern and northern Pakuashan are compared, no evidence for a significant difference in age of folding inception or in shortening rate is seen. If we now account for the N118°E direction of transport across the western foothills [e.g., *Dominguez et al.*, 2003a; *Yu et al.*,

Table 4. Model Parameters for Southern Pakuashan[a]

Parameters	Values	Uncertainties
Total shortening, m	850	90
λ (at surface)	−1.34E-04	7.08E-06
α		
Domain 1–2	5.92E-08	6.75E-10
Domain 2–3	1.90E-08	2.91E-10
Domain 3–4	8.50E-08	1.18E-09
Domain 4–5	1.21E-10	1.09E-11
Domain 5–6	−2.33E-07	1.35E-08

[a]See Figure 10. Uncertainty calculations are detailed in Appendix D. See caption of Table 3 for numbers identifying dip domains.

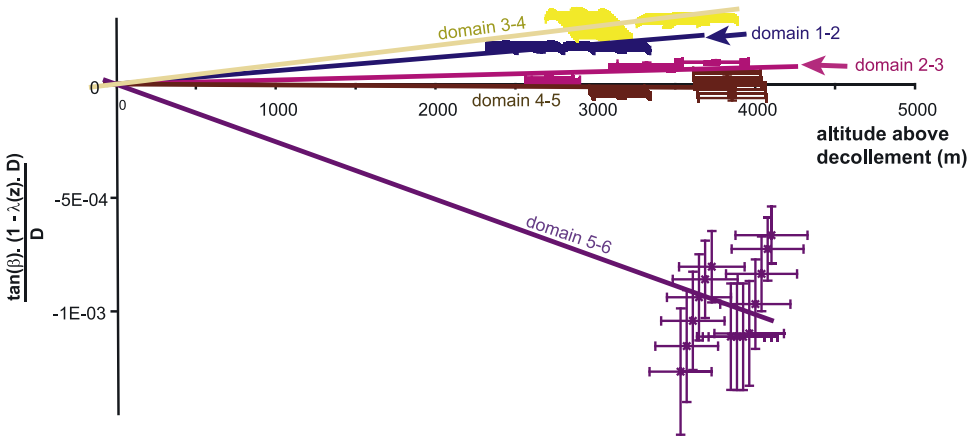

Figure 20. Plot of $[\tan(\beta_i)(1 - \lambda(z)D)]/D$ as a function of altitude z above the decollement for southern Pakuashan. See Figure 17 caption for further details.

1997; *Yu et al.*, 2001] and consider the data from both transects across Pakuashan, we estimate the total finite shortening to 1010 ± 160 m, the shortening rate to 16.3 ± 4.1 mm/yr, and the age of folding inception to 62,200 ± 9600 years (Figure 22). We assume that lateral transfer of material out of the direction of transport is negligible. Rather than the southward propagation of the anticline suggested by *Delcaillau et al.* [1998], the difference of morphology of southern and northern Pakuashan probably reflects different structural architectures (Figures 10 and 15) that could be partly related to the complex geometry of the underthrusting Chinese margin in this area.

6. Discussion

6.1. Applicability of the Fold Model of *Bernard et al.* [2007]

[39] The Changhua fault started to localize and propagate upward to depths of ~1700 m (Figure 8). The tilt of the

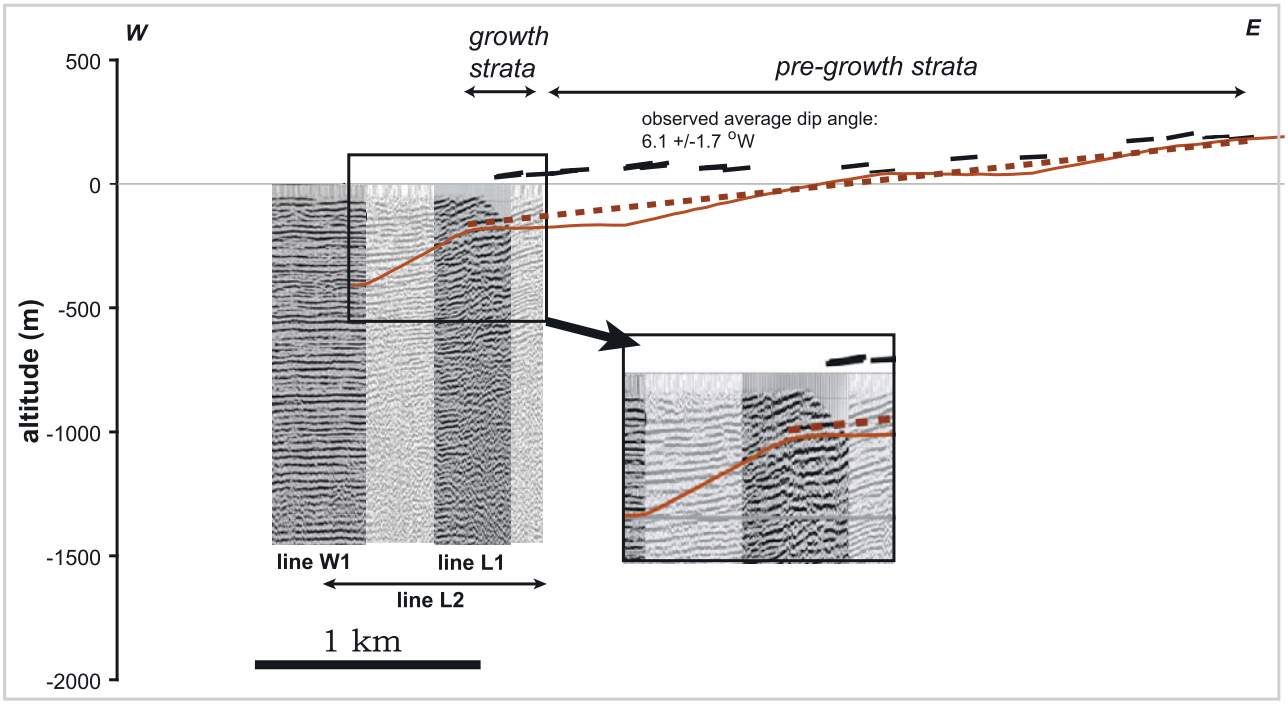

Figure 21. Close-up view of the structural measurements and shallow seismic data from the forelimb of northern Pakuashan. Pregrowth layers show a homogeneous dip angle over most of the forelimb, with an average value of 6.1° ± 1.7°W (dashed line), consistent with reflectors observed on line L1 (Figure 6). Significant lateral variations in the geometry of the structures are suggested from slightly steeper dip angles observed on the easternmost portion of line L2 and from the geometry of pregrowth layers as predicted from the fold model derived from our interpretation of the seismic profiles along the Tatu Hsi (solid line). In particular, the steeply dipping panel at the front, as revealed in the shallow seismic profiles of *Wang et al.* [2003], is not particularly observed along our transect. We therefore only rely in our analysis on dip angles observed exactly along the section surveyed in the field (Figure 6).

Table 5. Cumulative Shortening Retrieved for the Layers Surveyed in the Field[a]

Layer	Acquired Dip, deg	Error	Predicted Dip, deg	Error	Shortening, m	Error
Southern Pakuashan (N(90 ±5)E Direction)						
Strath of the 30,950 years B.P. old terrace[b]	3.0	0.4	5.9	3.5	457	153
Lateritic terrace P4[b]	2.2	1.0	5.9	3.5	338	140
Lateritic terrace P2[b]	1.7	1	5.9	3.5	265	141
Northern Pakuashan (N(78 ±3)E Direction)						
BC1	−7.5	1.0	−6.1	1.7	966	236
BC2	−7.2	1.0	−6.1	1.7	939	224
BC3	−5.5	1.0	−6.1	1.7	726	144
BC4	−5.1	1.1	−6.1	1.7	682	114
BC5	−4.7	1.2	−6.1	1.7	622	91
BC6	−6.7	0.8	−6.1	1.7	873	222
BC7	−5.2	3.7	−6.1	1.7	696	195
BC12	−6.3	0.7	−6.1	1.7	822	224
0906-1	−8.2	0.5	−6.1	1.7	1047	316
0906-6[b]	−2.0	2.0	−6.1	1.7	277	162
0906-7	−4.8	0.9	−6.1	1.7	640	134
0906-8	−6.0	0.6	−6.1	1.7	790	216
0906-9	−6.8	0.4	−6.1	1.7	883	277
0906-10	−4.8	0.0	−6.1	1.7	635	240
0906-11	−3.4	0.4	−6.1	1.7	457	129
0907-6	4.8	0.3	5.9	3.1	657	209
0907-9	6.0	1.6	5.8	3.1	825	116
Lateritic terrace[b]	2.9	1.0	9.1	3.1	270	115

[a]Positive dips plunge to the east, and negative values plunge to the west. Layers showing some complexities (faulted areas, complex geometry of the surveyed contact, etc.) or for which dip angles were too flat are not considered here.
[b]Growth layers or geomorphic surfaces.

lateritic surfaces (Figure 5) implies that the Pakuashan anticline still deforms by pure shear, at least near the surface. It can therefore be compared to the advanced stage of folding observed in the sandbox experiment of *Bernard et al.* [2007] after 3.4 mm of shortening, when deformation starts getting localized at depth. At this stage of the experiment, the deformation pattern becomes more complex, with two subtle shear bands in the forelimb of the fold, but incremental displacements can still be accounted for by the pure shear analytical expressions. *Bernard et al.* [2007] have tested the approach followed for the present case study, by calibrating analytical expressions from the synthetic finite structure obtained at this stage of folding, and by testing them against actual observed incremental displacements. Calculated displacements are found to be in good agreement with the observed values, except around the shear bands developing in the forelimb. In this case, calculated values underestimate the actual displacements by 10%. Should this apply to Pakuashan, then this may explain why the growth layer from the forelimb of the northern transect tends to lower the shortening rate (Figure 22, bottom) in light of the youngest pregrowth layer. Neglecting this growth layer implies a shortening rate on the Changhua fault of 17.3 mm/yr, in this case from only the lateritic terrace dated in the north by sample AYS15 (Figure 6) and from the three terraces on the backlimb of the southern transect. This rate is still within the error limits of the present estimate. Initiation of localization of the fault should therefore not significantly impact our results.

6.2. Morphologic Evolution of the Pakuashan Anticline

6.2.1. Morphology of the Pakuashan Anticline and Age of the Topography

[40] The kinematic fold model derived from the present study can be used to assess how sedimentation, uplift and erosion, have jointly created the observed topography and morphology. We model here the structure predicted by taking into account subsidence of the footwall and foreland sedimentation. We assume a constant sedimentation rate of 2.5 mm/yr, as derived in Figure 9. Folding starts at 62 ka, and this model reproduces the deposition and subsequent deformation of growth strata. Figure 23 shows the prediction of the model for the northern transect along the Tatu Hsi river. Sedimentation exceeds uplift near the frontal most part of the fold and on the eastern side of the backlimb (Figure 23a). The competition between uplift and sedimentation thus determines the width of the topographic expression of the fold. Growth strata are only found in these areas where sedimentation rate exceeds uplift. Also it provides an explanation as to why the fold structure extends below the Taichung Basin (Figure 15). These observations also apply to the southern transect across Pakuashan (Figure 24a), although the growth strata area within the backlimb is more limited. A larger fraction of the backlimb is buried under the basin in northern Pakuashan, whereas most of the backlimb is morphologically expressed in the southern area. This simple exercise illustrates how sedimentation and structurally controlled tectonics and uplift can contribute to produce different morphologies with similar kinematics of shortening.

[41] In a forward model, we mimic the deposition of an alluvial terrace across the fold at 19 ka and 21 ka for the southern and northern transects, respectively, equivalent to the observed lateritic surfaces. The predicted geometry of these terraces closely mimics the present topography of the fold for both sections (Figures 23b and 24b), although the predicted pattern for the 21 ka old surface to the north is slightly higher than the observed topography, indicating that most of the terrace has only recently been eroded away (Figure 23b). This is consistent with the Pakuashan anticline

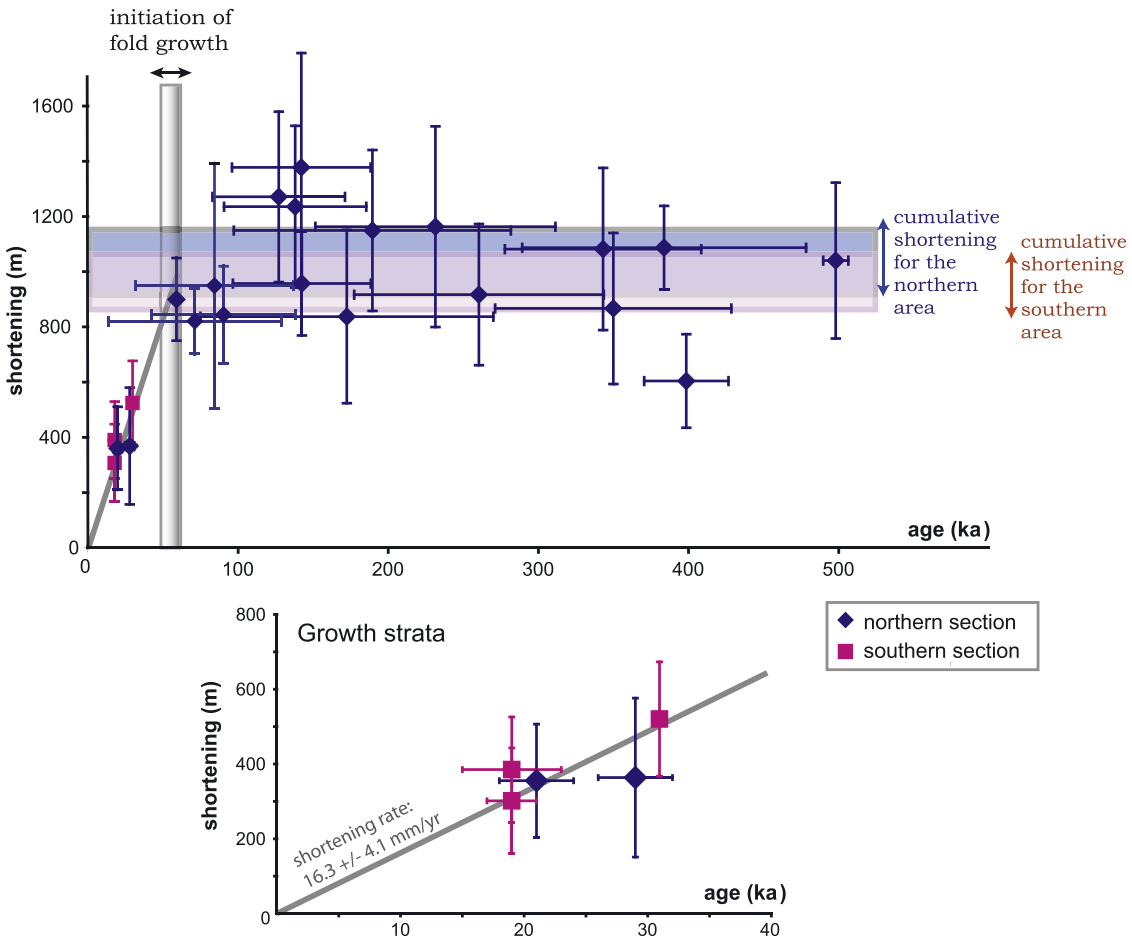

Figure 22. (top) Cumulative shortening versus age of the strata surveyed in the field, combining data for northern (blue) and southern (red) Pakuashan along the N118°E direction of tectonic transport. Cumulative shortening is calculated by converting acquired dip angles using equations (3) and (4) (Table 5) and by unprojecting these results obtained along sections A-A′ and B-B′ onto a N118°E direction. Ages were obtained from OSL dating or calculated from sedimentation rates and stratigraphic thicknesses (Figure 7). The kinematics is consistent from north to south, with a shortening rate of 16.3 ± 4.1 mm/yr. (bottom) Shortening versus age for dated growth layers.

being nearly capped by the remnants of these lateritic surfaces to the south rather than to the north (Figure 2). The pattern of Figures 23b and 24b also implies that the present topography only reflects the cumulative deformation over the past ~20 kyr, and that almost all the topography created prior to the last glacial maximum has been eroded away. We cannot estimate whether the topography was removed during a period of particular intense erosive climate ~20 kyr ago, or whether erosion prior to that had continuously prevented the emergence of an anticlinal ridge. In any case, erosion was possibly enhanced ~20 kyr ago because of a low stand sea level (~130 m below present sea level in the Taiwan area, see compilation by *Lai and Hsieh* [2003]). Finally, the differences in uplift rates along the two sections (Figures 23a and 24a) are related to the fold structure rather than to varying kinematics, and we propose that they generate the lateral variations in the fold morphology (Figure 2). In particular, lower uplift rates to the north may be responsible for the more dissected morphology.

[42] The system of former imbricate fluvial terraces within southern Pakuashan (Figures 4 and 5) further elucidates interaction between erosion and uplift. In particular, the estimated ~20 kyr long time lag separating the oldest (P1) and youngest (P3) terraces certainly represents the time needed before total defeat of the Choushui Hsi river in this area. On the basis of these estimated ages, our model predicts a differential incision between P1 and P3 of ~220 m at most, too high in view of the observed ~150 m elevation difference (Figure 5a). This is certainly because structural lateral variations may prevent from applying the model calibrated along the Choushui Hsi to terraces as far north as P1. Indeed, such structural changes relative to the transect along the Choushui Hsi are suggested by the abrupt change in the fold morphology at the level of P1 (Figures 2 and 4).

6.2.2. Balance Between Tectonic Uplift, Fluvial Incision, and Hillslope Erosion

[43] River incision since the inception of folding can be estimated by comparing the topography predicted by the

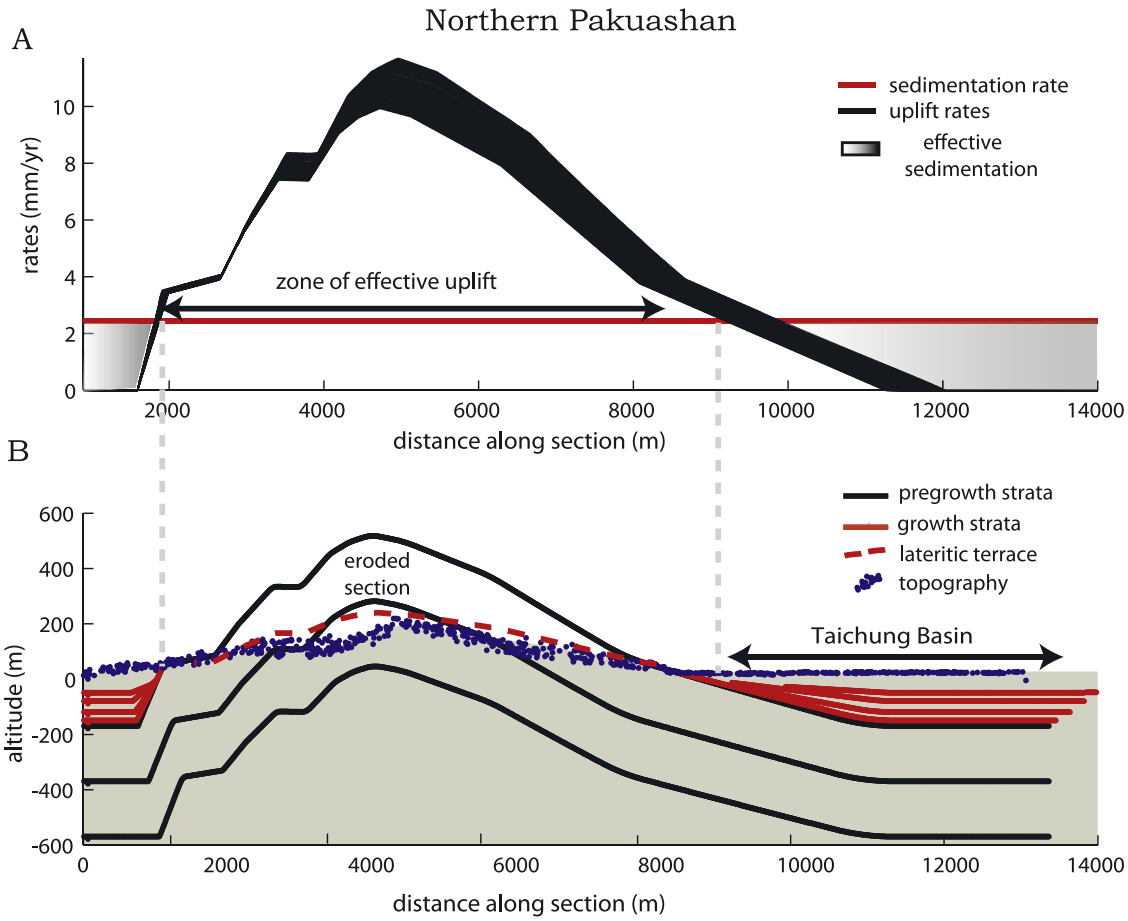

Figure 23. Fold growth and footwall subsidence predicted for northern Pakuashan. An average sedimentation rate of 2.5 mm/yr is assumed. (a) Uplift versus sedimentation rates predicted by our model. Where subsidence exceeds uplift (shaded areas), sedimentation prevails and the deposition of growth strata is possible. (b) Incremental growth of the northern Pakuashan anticline predicted by our model. Finite deformation is recorded by pregrowth strata (black), while incremental shortening is documented by growth strata (red). The red dashed line across the whole fold represents the deformed geometry of a 21 ka layer, equivalent to the lateritic surfaces capping the northern Pakuashan anticline.

model incorporating footwall subsidence with the present river valley geometry. Along the Tatu river, the eroded cross-sectional area (Figure 23) yields an incision rate of 4.2 mm/yr averaged over the fold width, with a maximum value of 8.3 mm/yr along the axial zone. Along the Choushui river, to the south, it suggests higher average incision rates of 8.7 mm/yr, with a maximum of 15.1 mm/yr along the fold axis. These estimates are similar, although lower for the northern section, to the 7 to 16 mm/yr river incision rates proposed by *Dadson et al.* [2003] within the southwestern foothills. As rivers can adjust their width to modulate their erosive power [*Lavé and Avouac*, 2001], they are more likely to keep pace with uplift induced by tectonics, in excess of the base level rise resulting from foreland sedimentation. During the last glacial low stand, high erosion rates might have prevailed over Pakuashan, because the ubiquitous lateritic fluvial deposits indicate that the Tatu and the Choushui Hsi were eroding the whole fold area. During sea level (and thus river base level) rise over the last ~20 kyr, the width of these two rivers had to narrow to maintain an erosive power sufficient to cross the frontal most active fold. Within the fold, lower erosion rates (by comparing predicted and observed topography) are responsible for its morphological expression. If climate and tectonic factors are kept constant, topography should evolve toward a steady state geometry characterized by slopes being steep enough for hillslope processes to be at pace with tectonic uplift and river incision. Preservation of the ~30 to ~19 kyr old lateritic terraces indicates that such a state has not yet been achieved since the last major climate epoch. The characteristic time needed to achieve a morphological steady state is therefore of the order of a few tens of thousand years in this particular case example.

7. Conclusion

[44] In this study, we model the incremental growth of the Pakuashan anticline above the Changhua blind thrust by combining the finite structure of the fold deduced from seismic profiles with the geometry of dated growth strata.

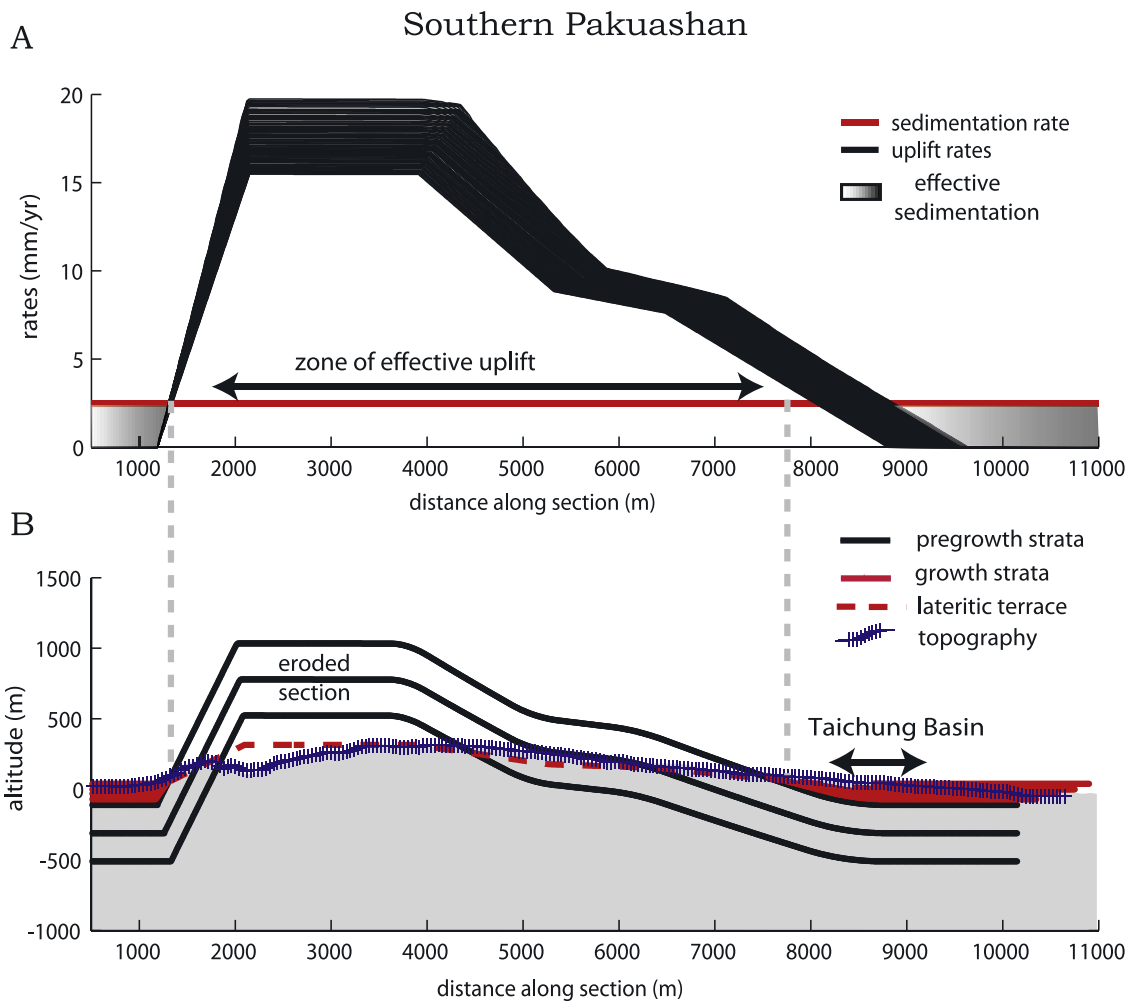

Figure 24. Same as Figure 23, but for southern Pakuashan. (a) Uplift versus sedimentation rates. (b) Incremental growth of the southern Pakuashan anticline. The predicted geometry of the 19 ka lateritic terrace (dashed red line) mimics well the present topography (blue dots).

We use the pure shear fold model of *Bernard et al.* [2007], which provides simple analytical expressions to model incremental fold growth as well as the finite fold structure in the case of a fault tip fold. Contrary to the trishear fault propagation model, which is another example of a parameterized pure shear fold model [*Allmendinger*, 1998; *Allmendinger and Shaw*, 2000; *Erslev*, 1991; *Zehnder and Allmendinger*, 2000], this model does not require an explicit account on the fault geometry or on the kinematics at depth. Therefore it cannot be used to make any inference about fault propagation or fault geometry. However, it offers a powerful and simple tool to estimate the shortening history across a fold using growth and pregrowth strata as well as deformed geomorphic markers. We find that deformation across Pakuashan initiated 62,200 ± 9600 years ago, with a shortening rate of 16.3 ± 4.1 mm/yr. Combined with constraints on the foreland sedimentation, our model shows how the present morphology of the Pakuashan anticline has resulted from the combination of uplift and erosion by river incision or hillslope processes. This study is the first application of this analytical fold model to a natural setting and we anticipate its application to a variety of other folds formed above blind thrust faults.

Appendix A: Seismic Profiles Analysis

A1. Northern Transect

[45] In the case of *Chen*'s [1978] profile, we convert the vertical scale from traveltimes to depths using the average velocities inferred from well shooting on PKS-1 [*Chen*, 1978] and from seismic refraction investigations [*Sato et al.*, 1970]. These velocities are thought to be more accurate than the slightly lower velocities (up to ~20%) obtained from the seismic reflection survey [*Chen*, 1978]. The seismic profile is segmented in three main subsets determined by a homogeneous or comparable velocity. The first subset comprises the top of the Toukoshan Formation down to a traveltime of 1059 ms and is attributed a velocity of 2434 m/s. The second one consists mainly of the lower Toukoshan Formation and most of the Cholan Formation. It goes from the base of the first subset down to the 1770 ms reflector and has a velocity of 3231 m/s. All deeper layers

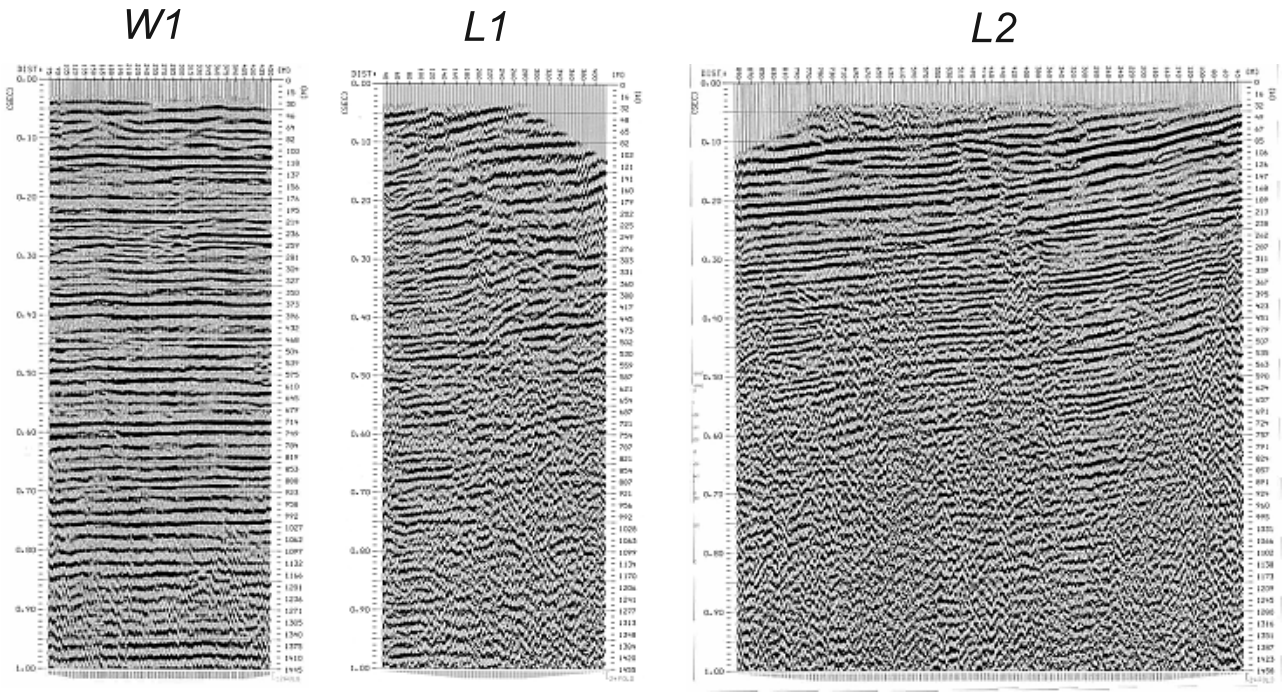

Figure A1. Shallow seismic profiles conducted in the northern Pakuashan area (Figure 6). Line W1 shows no deformation and thus constrains the westernmost limit for the Pakuashan anticline. Lines L1 and L2 show dipping layers providing constraints on the subsurface structures at the front.

are attributed a velocity of 4200 m/s. This velocity can be too high for Miocene series, but this does not impact our analysis because all deformation associated with folding occurs at shallower depths. This conversion is only approximate, but is found to predict depths for the different strata that are consistent with those observed on the well PKS-1 (see section A3). In the case of *Chang*'s [1971] profile we assume that the depth conversion was performed in the source paper using the same velocities. On the more recent profile of *Wang et al.* [2002], the velocities inferred for depth conversion are ~10% higher than those known in the western plain area. Therefore we reduce the vertical scale by this same amount. This correction applies mainly for the shallower strata, and is realistically not totally appropriate for levels deeper than ~4200 m.

A2. New Shallow Seismic Investigations in Northern Pakuashan: Data Processing

[46] In this study, shallow seismic investigations were conducted on the frontal most portion of our field area in northern Pakuashan. The equipments were (1) an EWG-III weight drop impact pulse generator for the source signal, (2) an OYO 40 Hz geophone receiver, and (3) a GEODE 144 channel seismograph to record the signal. The acquisition geometry used end-on shooting with the following survey parameters: (1) 6 m source interval, (2) 2 m receiver interval, (3) 100 m near offset, (4) fold of 24, (5) 0.25 ms sampling rate, and (6) 40 Hz low-cut filter. Because of traffic noise associated with highway 74, field work was conducted at night. The data processing follows standard procedures for CDP data, except for additional emphasis on some dip filters to suppress strong ground rolls. The frequency range of the seismic signals is 50–150 Hz. Depths are obtained by converting time to depth using a layered velocity model based on the stacked velocities of the best seismic line obtained in this experiment and by using the Dix equation (1) 1750 m/s for traveltime ranges between 0 and ~100 ms, (2) 2200 m/s from ~100 to ~300 ms, (3) 2600 m/s between ~300 and ~500 ms, and (4) 3300 m/s between ~500 and ~1000 ms. The mean velocity of 2621 m/s for depths between 0 and 1650 m, is similar to the velocities in the same depth range inferred from previous studies in the area. The seismic lines are displayed without interpretation in Figure A1.

A3. Uncertainties on Depths and Dips Extracted From Seismic Profiles

A3.1. Uncertainties on Depths

[47] Uncertainties on the depth of the reflectors relate primarily to the uncertainties on the velocity model used to convert times into depth. To estimate these errors, we compare depths of well-defined layers as estimated from the seismic profiles and from the available well logs. Results are illustrated in Table A1 for the cases of *Chen*'s [1978] and *Hung and Suppe*'s [2002] profiles, which have been compared to the PKS-1 [*Chang*, 1971] and TC-1 (J.-H. Hung, personal communication, 2005) wells, respectively. Depths do not differ by more than 5.2% and generally agree by ~3–4%. The agreement is particularly good, by 0.05% for the shallower reflectors in the northern area. A direct comparison with well data is not possible for each seismic line. We assume that the comparison made here holds for all the profiles used in this study. We thus consider a maximum error of 5.5% on the depths inferred from the seismic profiles.

Table A1. Error Estimate on the Position of Different Reflectors Observed From *Chen*'s [1978] and *Hung and Suppe*'s [2002] Profiles Across Northern and Southern Pakuashan[a]

Formation	*Chen*'s [1978] Profile Versus PKS-1	*Hung and Suppe*'s [2002] Profile Versus TC-1
Cholan	0.05%	-
Chinshui	5.2%	4.2%
Kueichulin	3.9%	5.2%
Talu Shale	3.8%	-
Shihti	4.2%	-
Pre-Miocene	1.0%	-

[a]Based on the positions observed in the PKS-1 [*Chang*, 1971] and TC-1 (J.-H. Hung, personal communication, 2005) wells, respectively. The top of the different formations has been considered. Predicted depths are in good agreement with the observed ones, with a maximum error of 5.2%.

A3.2. Uncertainties on Dips

[48] Our analysis requires estimation of dip angles of subsurface layers. We select and digitize only well-defined reflectors. The uncertainty on the dip angle arises from the errors on the horizontal and vertical distances separating consecutive points along the digitized reflectors. It therefore depends on the uncertainty on the strike of the considered layer (for the horizontals) and on the depth conversion of the seismic profile (for the verticals). Uncertainties on dips are calculated accordingly by partial derivatives taking into account the errors on the fold axis direction and on the depths inferred from the seismic profiles. This yields an error of 2.7% on the dip angles for most of the data retrieved for northern Pakuashan. The uncertainty is larger (about 11.5%) for the dip angles derived from the more oblique profiles of *Chang* [1971] and *Wang et al.* [2002]. In the case of the southern area, the uncertainty on the dip angles is estimated to 5.4%.

Appendix B: Field Data Acquisition

B1. Field Survey Methodology

[49] To measure bedding attitude and position, we used a real-time kinematic (RTK) GPS system, the Trimble 5700© RTK GPS, equipped with a Trimble Zephyr© antenna (for more information on the system, see http://trl.trimble.com/docushare/dsweb/Get/Document-6785/5700WPertkE.pdf and http://trl.trimble.com/docushare/dsweb/Get/Document-140051/Spec_Sheet_-_R7_-_English.pdf). The RTK GPS system involves two units kept in radio contact: a fixed one, the base, and a mobile one, the rover. The surveyed points are measured with the rover unit and the uncertainty on the position relative to the base station is quite low (within about 1 cm in the verticals and even better in the horizontals). These differential measurements allow for very precise positions because most of the errors inherent to GPS signals cancel out when only the local baselines are solved (except for multipath and receiver errors). In this study we had to move the base station several times to maintain radio contact but all measurements within each survey area (northern and southern Pakuashan) were tied to the same reference frame. When strata could not be reached easily, a geodetic laser range distance meter (Advantage system from LaserAtlanta©: for more information see http://www.laseratlanta.com/advantage.htm) equipped with a magnetic compass was used in combination with our RTK GPS system. The instrument measures distance, inclination and azimuth of the laser ray from the shooting point measured with the RTK GPS system to the targets.

[50] The field measurements were finally all tied to the 40-m resolution digital elevation model (DEM), using ground control points. Only a rigid translation was applied. This step leads to significant corrections of the measured elevations by 22.5 ± 0.2 m and by −2.1 ± 0.7 m in the northern and southern areas, respectively. The topography and the geometry of the preserved lateritic terraces were extracted from the DEM (Figures 4 and 6).

B2. Uncertainties on Positions and Dip Angles

[51] The uncertainties, at the 95% confidence level, on the positions measured from the RTK GPS are of 1 cm + 1 ppm of the signal RMS for horizontal coordinates, and of 2 cm + 1 ppm of the signal RMS for the vertical coordinates. In the case of the distant targets measured from the laser system, errors associated with the laser were added to those related to the RTK GPS measurement of the position of the shooting point. Uncertainties on the distance taken from the laser are of the order of 3 to 5 cm but we rather use a value of 15 cm in our calculations since field work was performed during the wet season. The inclinometer and the magnetic compass yield uncertainties of 0.4 and 0.3°, respectively. Since the laser height was measured with a meter stick, we assign it a maximum uncertainty of 2.5 mm (half a graduation). Finally, transposing these measurements to the DEM generates an additional error of 0.2 to 0.7 m in the vertical coordinates.

[52] The azimuth of the vertical plane tangent to the outcrop (generally a roadcut) and the plunge of the layer within this plane (the apparent dip angle) is determined from a least squares fitting algorithm [*Lybanon*, 1984] that takes into account all the uncertainties on the single points surveyed along each strata. This algorithm is implemented into an easy-to-use routine by T. Hubert and S. Mellema (2002) (for more information: http://physics.gac.edu/~huber/fitting/), and provides uncertainties on the results with a 95% confidence level. The apparent dip angles are used to estimate the real dip angles by assuming a N168 ± 3°E and N90 ± 5°E general strike for northern and southern Pakuashan, respectively. Uncertainties on the results are then calculated by the partial derivative method. We estimate that these uncertainties correspond to a 95% confidence level although the partial derivative method maximizes the calculated uncertainties.

Appendix C: OSL Dating

[53] Luminescence dating [*Aitken*, 1985, 1998] is based on the fact that (1) decay of natural radioactivity from the ^{238}U, ^{232}Th, and ^{40}K chains creates a natural radiation field which as a first approximation remains constant through time and (2) minerals, such as quartz and feldspar, acquire a luminescence signal due to exposure to this ionizing radiation. The intensity of luminescence is proportional to the absorbed dose and is thus a function of time. In the case of sediments, preburial exposure of mineral to day light during weathering and transport removes the geological lumines-

Table C1. Details for the Processed OSL Samples[a]

Sample	Mineral	Size, μm	Method	U, ppm	Th, ppm	K,%	DR, Gyr/kyr	P, Gyr	Disks	a	Age, ka
Pakua1-TL	Qtz	90–150	SAR	2.6 ± 0.7	12.1 ± 2.3	2.4 ± 0.12	3.5 ± 0.3	67.5 ± 14.6	7	-	19 ± 4
Pakua2-TL	Feld	4–11.	MAR	2.8 ± 1	17.6 ± 3.7	2.79 ± 0.14	5.1 ± 0.6	649 ± 214	26	0.040	128 ± 44
Pakua3-TL	Feld	4–11.	MAR	3.2 ± 0.9	12.1 ± 3.3	1.89 ± 0.09	3.9 ± 0.5	558.7 ± 169	28	0.040	143 ± 46
Pakua4-TL	Qtz	90–150	SAR	2.1 ± 0.4	12.1 ± 1.3	1.7 ± 0.08	2.8 ± 0.2	81.5 ± 1.4	88	-	29 ± 3
Pakua5-TL	Feld	4–11.	MAR	4.1 ± 0.6	12.4 ± 2	2.4 ± 0.12	4.5 ± 0.4	1525 ± 266	28	0.030	340 ± 66
AYS15[b]	Qtz	150–210	SAR	1.3 ± 1	16 ± 3.6	1.9 ± 0.1	2.9 ± 4	112 ± 8.7	19	-	21 ± 3
AYS-16[b]	Qtz	125–150	SAR	3.1 ± 0.1	10.6 ± 0.4	1.5 ± 0.08	2.6 ± 0.2	50.3 ± 2.9	33	-	19 ± 1.8

[a]Luminescence signal of quartz (Qtz) or feldspar (Feld) grains were analyzed using single aliquot regeneration (SAR) or multiple aliquot regeneration (MAR) protocols. Moisture content was assumed to be 15 ± 5%. Dose rates (DR) are calculated based on the environmental irradiation. In the case of the SAR method, average of all obtained paleodoses (P) has been considered for the samples, except for AYS15 and AYS16.

[b]Minimum ages were considered because of the scattered distribution obtained for their dose rates. Mean ages for AYS15 and AYS16 are 38 ± 6 and 24 ± 7 ka, too old in view of other independent constraints (Figures 5 and 22).

cence. On burial, the daylight exposure ceases and a reacquisition of luminescence due to the ambient environmental radiation field is initiated. This method can therefore be used to directly date the age of sediment burial. In practice, the cumulative dose is measured from the luminescence produced by the minerals upon thermal or optical laboratory stimulation. The age of sediment burial is then calculated using the equation

$$\text{age} = (\text{acquired luminescence}) / (\text{annual rate of luminescence acquisition})$$

This can be converted into radiation dose units given the equation

$$\text{age(ka)} = \text{paleodose(in Gyr)} / \text{annual dose rate(in Gyr/kyr)}$$

where the ''paleodose'' is the radiation level associated with the observed luminescence signal. The ''annual dose rate'' is determined by measuring the concentration of radionuclides ^{238}U, ^{232}Th and ^{40}K, and by using standard conversion factors and appropriate water content values. The contribution of the cosmic rays is also added [*Aitken*, 1985, 1998].

[54] In the present study, a total of 7 samples were analyzed (Tables 2 and C1). They were collected after cleaning the outcrop surfaces of the strata being sampled. After that, metal pipes were inserted into the sediments under dark conditions to ensure that the samples did not experience any day light exposure during sampling and transport to the laboratory. Samples Pakua1-TL, Pakua4-TL, AYS15 and AYS16 are mostly sands, and Pakua2-TL, Pakua3-TL and Pakua5-TL comprised sandy silts. Consequently, Pakua1-TL, Pakua4-TL, AYS15, and AYS16 were analyzed using coarse grain quartz and the three others were analyzed using the fine grain technique. For the former 4 samples, the sample pretreatment comprised a sequential reaction with 10% HCl and 30% H_2O_2 to remove carbonates and organic matter, followed by sieving to obtain 90–150 μm grains. A density separation using Na-Polytungstate ($\rho = 2.58$ g/cm^3) was carried out to separate quartz and feldspar minerals. The quartz fraction was then etched with 40% HF for 80 min followed by 12 N HCl for 60 min to remove the alpha skin and residual feldspars. A portion of these grains was tested for purity using the infrared stimulated luminescence. The grains were subsequently mounted on stainless steel discs using Silkospray™. The quartz measurements were done on Riso TL-DA-15 reader with blue LED ($\lambda = 470 \pm 20$ nm) for stimulation. The detection optics comprised Hoya U340 and Schott BG-39 filters coupled with 9635 QA photo multiplier (PMT) tube. Laboratory irradiation was realized using a ^{90}Sr/^{90}Y source, delivering a dose rate of ~7.5 Gyr/min. Single aliquot regeneration (SAR) protocol allowed for computing the corresponding paleodoses [*Murray and Wintle*, 2000]. Given the relative overall antiquity of the ages, we generally used the mean of the distribution of SAR ages, except for AYS15 and AYS16. In fact, these two samples gave a scattered distribution of their respective dose rates, suggesting that they had not been totally bleached during deposition. *Chen et al.* [2003] reported similar problems for samples from western Taiwan, and attributed them to the fast deposition of sediments in the region. For these reasons, minimum ages for AYS15 and AYS16 are considered more meaningful for our analysis. On the other hand, the samples from silt-dominated units (Pakua2-TL, 3-TL and 5-TL) were processed separately to get 4–11 μm grains. In this case, samples after treatment by HCl and H_2O_2 were deflocculated in 0.1 N sodium oxalate, and subsequently washed and then suspended in acetone for Stoke's separation of the 4–11 μm fine silt fraction. The separated fraction was resuspended and equal volumes were then pipetted onto aluminum discs in cylinders with a column of acetone over them. The acetone was then evaporated at >45°C, after what a thin layer was left on the discs. Infrared stimulated luminescence (IRSL) measurements using infrared diodes ($\lambda = 880 \pm 80$ nm) were carried out using a Daybreak 1150 TL-OSL reader. Detection optics comprised Corning 7–59 and Schott BG-39 filters for IRSL, which were used with all the measurements done on a Daybreak 1100 reader. The β irradiation was done separately using ^{90}Sr/^{90}Y source having a dose rate of 2.44 Gyr/min. Alpha irradiation was done using Americium-241 to compute the 'a' value. Multiple aliquot additive dose method with late light subtraction allowed for computing the paleodoses. A preheat of 240°C for 10 s removed the unstable signal. For dose rates, ^{238}U and ^{232}Th concentrations were measured by ZnS (Ag) thick source alpha counting using Daybreak 583 alpha counters. ^{40}K concentration was estimated by gamma spectrometry using NaI (Tl) crystal and a multichannel pulse

height analyzer. The errors were computed using standard error protocols.

Appendix D: Uncertainties on Finite Shortening and on Model Parameters

D1. Uncertainty on Total Shortening

[55] Total shortening across northern and southern Pakuashan is determined by the excess area method [*Epard and Groshong*, 1993]. Surfaces defined by deformed levels are determined by tracing reflectors across the whole anticline. To assess uncertainties on their areas, we use the uncertainties estimated for the dip angles retrieved from seismic profiles (Appendix A). Minimum and maximum areas around each one of the previous surfaces are estimated, by considering minimum and maximum possible dip values within each dip domain. The probability that observed dips are at their maximum (or minimum) values within each domain all along a reflector is expected to be negligible, so that this approach maximizes uncertainties on the excess areas. The weighted least squares regression of *Lybanon* [1984] (Appendix B), is used to assess the finite shortening and the uncertainty on this value from equation (5) (Figure 16). Uncertainties provided by this regression correspond to a 95% confidence level.

D2. Uncertainties on Model Parameters

[56] The parameter $\lambda(z)$ is retrieved for different depths from the observed fold width (Figure 15) and equation (1). Uncertainty on the fold width is considered to result from the error on the fold axis direction. The uncertainty on $\lambda(z)$ is then calculated by partial derivatives.

[57] To determine α_i for each domain i, dips acquired during fold growth are first calculated by correcting observed tilts from the inferred initial geometry (Figure 15). From equation (3), $[\tan(\beta_i)(1 - \lambda(z)D)]/D$ is calculated, taking into account the finite shortening across the fold and the $\lambda(z)$ values corresponding to the initial depth z of the reflector. Uncertainties on $[\tan(\beta_i)(1 - \lambda(z)D)]/D$ are calculated from errors on the input parameters using partial derivatives. A weighted least squares linear regression forced to the origin (Appendix B) is then applied to the observed trend of $[\tan(\beta_i)(1 - \lambda(z)D)]/D$ as a function of z in order to retrieve the α_i values for each domain as well as their respective uncertainties. The confidence level may be considered here to be of 95%, although partial derivatives maximize uncertainties.

Appendix E: Uncertainty on the Fold Model

[58] A "mean" model, considering the mean value of total shortening, of parameters α_i and $\lambda(z)$, and of initial dip angles is first obtained. To account for the effect of the uncertainties of these parameters on the fold model, we also consider extreme models, combining maximum and minimum possible values, respectively, of all parameters. Finally, extreme and mean models are combined together and subsequently compared to the observations from the seismic profiles to test the validity of the fold model. Uncertainties on the dips predicted by the model are derived from this analysis and correspond to the standard deviation of the distribution of the misfit between observations and predictions. They are most probably maximized since the probability that all parameters are all at their extreme values is small. Corresponding confidence levels are thus over 95%.

Appendix F: Errors on Shortening Rates

[59] Errors on cumulative shortening calculated from equations (3) or (4) are estimated based on the partial derivatives of these equations. In the case of the growth strata, a weighted least squares regression after [*Lybanon*, 1984] (Appendix B) is used to assess shortening rates, as well as their uncertainties, from cumulative shortening as a function of age. Since in our approach most uncertainties are overestimated by partial derivatives or by considering extreme cases, our final uncertainties on the ages of deformation inception and on the shortening rate most probably represent a confidence level over 95%.

[60] **Acknowledgments.** The Trimble 5700 RTK GPS system was provided by the CEA (France), and the laser distance meter was provided by Academia Sinica (Taiwan). We wish to thank O. Beyssac, J.-C. Hu, and R.-F. Chen for their valuable help in the field, as well as E. Thauvin for his help with the RTK GPS system. We are also indebted to A. Tyagi for his help in measuring the AYS series of OSL samples. Our study of southern Pakuashan was also made possible by J.-H. Hung, who kindly provided the data from the TC-1 well. This manuscript benefited from discussions with J. Suppe, S. Dominguez, and J. Malavieille and from the thoughtful and constructive reviews by J. Shaw, D. Burbank, and the Associate Editor, J. Dolan. These investigations were initiated thanks to a grant to J.P.A. from CNRS/INSU (France). This study was also partly funded by the Gordon and Betty Moore Foundation. This is Caltech Tectonics Observatory contribution 66.

References

Aitken, M. J. (1985), *Thermo-luminescence Dating*, 359 pp., Elsevier, New York.

Aitken, M. J. (1998), *An Introduction to Optical Dating: The Dating of Quaternary Sediments by the Use of Photon-Stimulated Luminescence*, 267 pp., Oxford Univ. Press, New York.

Allmendinger, R. W. (1998), Inverse and forward numerical modeling of trishear fault-propagation folds, *Tectonics*, *17*, 640–656.

Allmendinger, R. W., and J. H. Shaw (2000), Estimation of fault propagation distance from fold shape: implications for earthquake hazard assessment, *Geology*, *28*, 1099–1102.

Audet, D. M. (1995), Modelling of porosity evolution and mechanical compaction of calcareous sediments, *Sedimentology*, *42*, 355–373.

Avouac, J. P., P. Tapponnier, M. Bai, H. You, and G. Wang (1993), Active thrusting and folding along the Northern Tien Shan and late cenozoic rotation of the Tarim relative to Dzungaria and Kazakhstan, *J. Geophys. Res.*, *98*, 6755–6804.

Berggren, W. A. (1973), The Pliocene time scale: calibration of planktonic and calcareous nannoplankton zones, *Nature*, *243*, 391–397.

Berggren, W. A., et al. (1995), Late Neogene chronology: New perspectives in high-resolution stratigraphy, *Geol. Soc. Am. Bull.*, *107*, 1272–1287.

Bernard, S., J. P. Avouac, S. Dominguez, and M. Simoes (2007), Kinematics of fault-related folding derived from a sandbox experiment, *J. Geophys. Res.*, doi:10.1029/2005JB004149, in press.

Bonilla, M. G. (1975), A review of recently active faults in Taiwan, *U.S. Geol. Surv. Open File Rep.*, *75-41*.

Bonilla, M. G. (1999), A note on historic and Quaternary faults in western Taiwan, *U.S. Geol. Surv. Open File*, *99-447*.

Briais, A., P. Patriat, and P. Tapponnier (1993), Updated interpretation of magnetic anomalies and seafloor spreading stages in the South China Sea: Implications for the Tertiary tectonics of Southeast Asia, *J. Geophys. Res.*, *98*, 6299–6328.

Cattin, R., A. Loevenbruck, and X. Le Pichon (2004), Why does the coseismic slip of the 1999 Chi-Chi (Taiwan) earthquake increase progressively northwestward on the plane of rupture?, *Tectonophysics*, *386*, 67–80.

Chang, S. S. L. (1971), Subsurface geologic study of the Taichung Basin, Taiwan, *Pet. Geol. Taiwan*, *8*, 21–45.

Chang, S. S. L., and W. R. Chi (1983), Neogene nannoplankton biostratigraphy in Taiwan and the tectonic implications, *Pet. Geol. Taiwan*, *19*, 93–147.

Chen, H.-W., M.-M. Chen, and T.-S. Shih (2004), 1:50000 geological map of Taiwan,-sheet 24, Nantou, Central Geol. Surv. of Taiwan, Taipei.
Chen, J.-S. (1978), A comparative study of the refraction and reflection seismic data obtained on the Changhua plain to the Peikang Shelf, Taiwan, *Pet. Geol. Taiwan*, *15*, 199–217.
Chen, Y.-G., et al. (2003), Preliminary results of long-term slip rates of 1999 earthquake fault by luminescence and radiocarbon dating, *Quat. Sci. Rev.*, *22*, 1213–1221.
Chou, Y.-W., and H.-S. Yu (2002), Structural expressions of flexural extension in the arc-continent collisional foredeeep of western Taiwan, *Spec. Pap. Geol. Soc. Am.*, *358*, 1–12.
Covey, M. (1984a), Lithofacies analysis and basin reconstruction, Plio-Pleistocene western Taiwan foredeep, *Pet. Geol. Taiwan*, *20*, 53–83.
Covey, M. (1984b), Sedimentary and tectonic evolution of the Western Taiwan foredeep, Ph.D. thesis, 152 pp, Princeton Univ., Princeton, N. J.
Covey, M. (1986), The evolution of foreland basins to steady-state: Evidence from the western Taiwan foreland basin, *Spec. Publ. Int. Assoc. Sedimentol.*, *8*, 77–90.
Dadson, S. J., et al. (2003), Links between erosion, runoff variability and seismicity in the Taiwan orogen, *Nature*, *426*, 648–651.
Dahlstrom, C. D. A. (1990), Geometric constraints derived from the law of conservation of volume and applied to evolutionary models of detachment folding, *AAPG Bull.*, *74*, 336–344.
Delcaillau, B. (2001), Geomorphic response to growing fault-related folds: Example from the foothills of Taiwan, *Geodin. Acta*, *14*, 265–287.
Delcaillau, B., et al. (1998), Morphotectonic evidence from lateral propagation of an active frontal fold: Pakuashan anticline, foothills of Taiwan, *Geomorphology*, *24*, 263–290.
Dominguez, S., J. Avouac, and R. Michel (2003a), Horizontal coseismic deformation of the 1999 Chi-Chi earthquake measured from SPOT satellite images: Implications for the seismic cycle along the western foothills of central Taiwan, *J. Geophys. Res.*, *108*(B2), 2083, doi:10.1029/2001JB000951.
Dominguez, S., J. Malavieille, and J. P. Avouac (2003b), Fluvial terraces deformation induced by thrust faulting: an experimental approach to estimate crustal shortening velocity, paper presented at EGS-EAGU-EGU Joint Assembly, Nice, France.
Epard, J.-L., and R. H. J. Groshong (1993), Excess area and depth to detachment, *AAPG Bull.*, *77*, 1291–1302.
Epard, J.-L., and R. H. J. Groshong (1995), Kinematic model of detachment folding including limb rotation, fixed axial surfaces and layer-parallel strain, *Tectonophysics*, *247*, 85–103.
Erslev, E. (1991), Trishear fault-propagation folding, *Geology*, *19*, 617–620.
Horng, C.-S., and K.-S. Shea (1996), Dating of the Plio-Pleistocene rapidly deposited sequence based on integrated magneto-biostratigraphy: A case study of the Magida-Chi section, Coastal Range, eastern Taiwan, *J. Geol. Soc. China*, *39*, 31–58.
Hsu, S. K., et al. (1998), New gravity and magnetic anomaly maps in the Taiwan-Luzon region and their preliminary interpretation, *Terr. Atmos. Oceanic Sci.*, *9*, 509–532.
Huang, T. (1984), Planktic foraminiferal biostratigraphy and datum planes in the Neogene sedimentary sequence in Taiwan, *Paleogeogeogr. Paleoclimatol. Paleoecol.*, *46*, 97–106.
Hung, J.-H., and J. Suppe (2002), Subsurface geometry of the Sani-Chelungpu faults and fold scarp formation in the 1999 Chi-Chi Taiwan earthquake, *Eos Trans. AGU*, *83*(47), Fall Meet. Suppl., Abstract T61B-1268.
Lai, T.-H. and M.-L. Hsieh (2003), Late-Quaternary vertical rock-movement rates of the coastal plains of Taiwan, paper presented at Geological Society of Taiwan meeting, Taipei.
Lavé, J., and J. P. Avouac (2000), Active folding of fluvial terraces across the Siwaliks Hills, Himalayas of central Nepal, *J. Geophys. Res.*, *105*, 5735–5770.
Lavé, J., and J. P. Avouac (2001), Fluvial incision and tectonic uplift across the Himalayas of central Nepal, *J. Geophys. Res.*, *106*, 26,561–26,591.
Lee, C. T., and P.-S. Lin (2004), Active faults and seismic hazards in West Central Taiwan., paper presented at International Conference in Commemoration of 5th Anniversary of the 1999 Chi-Chi Earthquake, Taiwan, Central Geol. Surv., Taipei, Sept. .
Liew, P. M. (1988), Quaternary stratigraphy in western Taiwan: Palynological correlation, *Proc. Geol. Soc. China.*, *31*, 169–180.
Lin, A. T., A. B. Watts, and S. P. Hesselbo (2003), Cenozoic stratigraphy and subsidence history of the South China Sea margin in the Taiwan region, *Basin Res.*, *15*, 453–478.
Loevenbruck, A., R. Cattin, X. Le Pichon, M.-L. Courty, and S.-B. Yu (2001), Seismic cycle in Taiwan derived from GPS measurements, *C. R. Acad. Sci.*, *333*, 57–64.
Lybanon, M. (1984), A better least-squares method when both variables have uncertainties, *Am. J. Phys.*, *52*, 22–26.
Ma, H. F., C. T. Lee, Y.-B. Tsai, T.-C. Shin, and J. Mori (1999), The Chi-Chi, Taiwan earthquake: Large surface displacements on an inland thrust fault, *Eos Trans. AGU*, *80*, 605.
Mitra, S. (2003), A unified kinematic model for the evolution of detachment folds, *J. Struct. Geol.*, *25*, 1659–1673.
Mouthereau, F., O. Lacombe, B. Deffontaines, J. Angelier, and H. T. Chu (1999), Quaternary transfer faulting and belt front deformation at Pakuashan (western Taiwan), *Tectonics*, *18*, 215–230.
Murray, A. S., and A. G. Wintle (2000), Luminescence dating of quartz grain using an improved single-aliquot regenerative-dose protocol, *Radiat. Measur.*, *32*, 57–73.
Ota, Y., J. B. H. Shyu, Y.-G. Chen, and M.-L. Hsieh (2002), Deformation and age of fluvial terraces south of the Choushui river, central Taiwan, and their tectonic implications, *West. Pac. Earth Sci.*, *2*, 251–260.
Pathier, E., et al. (2003), Coseismic displacements of the footwall of the Chelungpu fault caused by the 1999, Taiwan, Chi-Chi earthquake from InSAR and GPS data, *Earth Planet. Sci. Lett.*, *212*, 73–88.
Sato, K., et al. (1970), Reports on the seismic refraction survey on land in the western part of Taiwan, Republic of China, *Pet. Geol. Taiwan*, *7*, 281–293.
Sella, G. F., T. H. Dixon, and A. Mao (2002), REVEL: A model for Recent plate velocities from space geodesy, *J. Geophys. Res.*, *107*(B4), 2081, doi:10.1029/2000JB000033.
Shaw, J. H., A. Plesch, J. F. Dolan, T. L. Pratt, and P. Fiore (2002), Puente Hills blind-thrust system, Los Angeles, California, *Bull. Seismol. Soc. Am.*, *92*, 2946–2960.
Shyu, J. B. H., K. Sieh, Y.-G. Chen, and C.-S. Liu (2005), Neotectonic architecture of Taiwan and its implications for future large earthquakes, *J. Geophys. Res.*, *110*, B08402, doi:10.1029/2004JB003251.
Simoes, M., and J. P. Avouac (2006), Investigating the kinematics of mountain building in Taiwan from the spatiotemporal evolution of the foreland basin and western foothills, *J. Geophys. Res.*, *111*, B10401, doi:10.1029/2005JB004209.
Simoes, M., J. P. Avouac, and Y.-G. Chen (2007), Slip rates on the Chelungpu and Chushiang thrust faults, inferred from a deformed strath terrace along the Dungpuna river, west central Taiwan, *J. Geophys. Res.*, doi:10.1029/2005JB004200, in press.
Suppe, J. (1983), Geometry and kinematics of fault-bend folding, *Am. J. Sci.*, *283*, 684–721.
Suppe, J., and D. A. Medwedeff (1990), Geometry and kinematics of fault-propagation folding, *Eclogae Geol. Helv.*, *83*, 409–454.
Suppe, J., G. T. Chou, and S. C. Hook (1992), Rates of folding and faulting determined from growth strata., in *Thrust Tectonics.*, edited by K. R. McClay, pp. 105–121, CRC Press, Boca Raton, Fla.
Suppe, J., C. D. Connors, and J.-F. Zhang (2002), Shear fault-bend folding., in *Thrust Tectonics and Hydrocarbon Systems*, edited by K. R. McClay, *AAPG Mem.*, *82*, 303–323.
Teng, L. S. (1987), Stratigraphic records of the late Cenozoic Penglai orogeny of Taiwan, *Acta Geol. Taiwan.*, *25*, 205–224.
Tsai, Y.-B. (1985), A study of disastrous earthquakes in Taiwan, 1683–1895, *Bull. Inst. Earth Sci. Acad. Sin.*, *5*, 1–44.
Wang, C. Y., et al. (2002), Structural mapping of the 1999 Chi-Chi earthquake fault, Taiwan, by seismic reflection methods, *Terr. Atmos. Oceanic Sci.*, *13*, 211–226.
Wang, C. Y., S.-Y. Kuo, W.-L. Shyu, and J.-W. Hsiao (2003), Investigating near-surface structures under the Changhua fault, west-central Taiwan by the reflection seismic method, *Terr. Atmos. Oceanic Sci.*, *14*, 343–367.
Yu, S.-B., H.-Y. Chen, and L.-C. Kuo (1997), Velocity field of GPS stations in the Taiwan area, *Tectonophysics*, *274*, 41–59.
Yu, S.-B., et al. (2001), Preseismic deformation and coseismic displacements associated with the 1999 Chi-Chi, Taiwan, earthquake, *Bull. Seismol. Soc. Am.*, *91*, 995–1012.
Yue, L. F., J. Suppe, and J.-H. Hung (2005), Structural geology of a classic thrust belt earthquake: the 1999 Chi-Chi earthquake Taiwan (M_w = 7.6), *J. Struct. Geol.*, *27*, 2058–2083.
Zehnder, A., and R. W. Allmendinger (2000), Velocity field for the trishear model, *J. Struct. Geol.*, *22*, 1009–1014.

J. P. Avouac, Tectonics Observatory, California Institute of Technology, MC 100-23, 1200 E. California Blvd., Pasadena, CA 91125, USA.
S. Bernard, Laboratoire de Géologie, CNRS, Ecole Normale Supérieure, 24 rue Lhomond, F-75005 Paris, France.
Y.-C. Chan, Institute of Earth Sciences, Academia Sinica, 128 Academia Road, Sec. 2, Nankang, Taipei 115, Taiwan.

Y.-G. Chen and M. Jaiswal, Department of Geosciences, National Taiwan University, P.O. Box 13-318, Taipei 106, Taiwan.

M. Simoes, Géosciences Rennes, CNRS-Université Rennes 1, Campus Beaulieu, F-35042 Rennes, France. (martine.simoes@univ-rennes1.fr)

A. K. Singhvi, Planetary and Geosciences Division, Physical Research Laboratory, Navrangpura, Ahmedabad 380 009, India.

C.-Y. Wang, Institute of Geophysics, National Central University, 300 Jhongda Road, Jhongli 32001, Taiwan.